IUCrJ
ISSN 2052-2525
PHYSICS | FELS

High-quality ultra-fast total scattering and pair distribution function data using an X-ray free-electron laser

Adam F. Sapnik,[a]* Philip A. Chater,[b] Dean S. Keeble,[b] John S. O. Evans,[c] Federica Bertolotti,[d] Antonietta Guagliardi,[e] Lise J. Støckler,[f] Elodie A. Harbourne,[g] Anders B. Borup,[f] Rebecca S. Silberg,[a] Adrien Descamps,[h] Clemens Prescher,[i] Benjamin D. Klee,[j] Axel Phelipeau,[k] Imran Ullah,[l] Kárel G. Medina,[l] Tobias A. Bird,[b] Viktoria Kaznelson,[f] William Lynn,[h] Andrew L. Goodwin,[g] Bo B. Iversen,[f] Celine Crepisson,[m] Emil S. Bozin,[n] Kirsten M. Ø. Jensen,[a] Emma E. McBride,[h] Reinhard B. Neder,[l] Ian Robinson,[o] Justin S. Wark,[m] Michał Andrzejewski,[p] Ulrike Boesenberg,[p] Erik Brambrink,[p] Carolina Camarda,[p] Valerio Cerantola,[p,q] Sebastian Goede,[p] Hauke Höppner,[r] Oliver S. Humphries,[p] Zuzana Konopkova,[p] Naresh Kujala,[p] Thomas Michelat,[p] Motoaki Nakatsutsumi,[p] Alexander Pelka,[r] Thomas R. Preston,[p] Lisa Randolph,[p] Michael Roeper,[k] Andreas Schmidt,[p] Cornelius Strohm,[k] Minxue Tang,[p] Peter Talkovski,[k] Ulf Zastrau,[p] Karen Appel[p] and David A. Keen[s]*

[a]Department of Chemistry, University of Copenhagen, Universitetsparken 5, 2100 Copenhagen Ø, Denmark, [b]Diamond Light Source, Diamond House, Harwell Science & Innovation Campus, Didcot, Oxford, United Kingdom, [c]Department of Chemistry, University Science Site, Durham University, South Road, Durham DH1 3LE, United Kingdom, [d]Dipartimento di Scienza e Alta Tecnologia and To.Sca.Lab, University of Insubria, Como, Italy, [e]Istituto di Cristallografia and To.Sca.Lab, CNR, Como, Italy, [f]Center for Integrated Materials Research, Department of Chemistry and iNANO, Aarhus University, Langelandsgade 140, 8000 Aarhus C, Denmark, [g]Department of Chemistry, Inorganic Chemistry Laboratory, University of Oxford, South Parks Road, Oxford OX1 3QR, United Kingdom, [h]School of Mathematics and Physics, Queen's University Belfast, University Road, Belfast BT7 1NN, United Kingdom, [i]Institute of Earth and Environmental Sciences, University of Freiburg, Freiburg, Germany, [j]HUN-REN Wigner Research Centre for Physics, Konkoly-Thege Miklós út 29-33, 1121 Budapest, Hungary, [k]Deutsches Elektronen-Synchrotron (DESY), Hamburg, Germany, [l]Friedrich-Alexander-Universität Erlangen-Nürnberg, Staudtstrasse 3, D-91058 Erlangen, Germany, [m]Department of Physics, Clarendon Laboratory, University of Oxford, Parks Road, Oxford OX1 3PU, United Kingdom, [n]Center for Solid State Physics and New Materials, Institute of Physics Belgrade, University of Belgrade, Pregrevica 118, 11080 Belgrade, Serbia, [o]London Centre for Nanotechnology, University College London, London WC1E 6BT, United Kingdom, [p]European XFEL, Holzkoppel 4, 22869 Schenefeld, Germany, [q]University of Milano-Bicocca, Piazza della Scienza 4, Milan 20126, Italy, [r]Helmholtz-Zentrum Dresden-Rossendorf (HZDR), Dresden, Germany, and [s]ISIS Facility, Rutherford Appleton Laboratory, Harwell Campus, Didcot, Oxford OX11 0QX, United Kingdom. *Correspondence e-mail: afs@chem.ku.dk, david.keen@stfc.ac.uk

Received 1 May 2025
Accepted 17 June 2025

Edited by T. Ishikawa, Harima Institute, Japan

Keywords: femtosecond studies; nanocrystals; pump–probe; time-resolved studies; XFELs; total scattering; pair distribution function.

Supporting information: this article has supporting information at www.iucrj.org

High-quality total scattering data, a key tool for understanding atomic-scale structure in disordered materials, require stable instrumentation and access to high momentum transfers. This is now routine at dedicated synchrotron instrumentation using high-energy X-ray beams, but it is very challenging to measure a total scattering dataset in less than a few microseconds. This limits their effectiveness for capturing structural changes that occur at the much faster timescales of atomic motion. Current X-ray free-electron lasers (XFELs) provide femtosecond-pulsed X-ray beams with maximum energies of ∼24 keV, giving the potential to measure total scattering and the attendant pair distribution functions (PDFs) on femtosecond timescales. We demonstrate that this potential has been realized using the HED scientific instrument at the European XFEL and present normalized total scattering data for $0.35\ \text{Å}^{-1} < Q < 16.6\ \text{Å}^{-1}$ and their PDFs from a broad spectrum of materials, including crystalline, nanocrystalline and amorphous solids, liquids and clusters in solution. We analyzed the data using a variety of methods, including Rietveld refinement, small-box PDF refinement, joint reciprocal–real-space refinement, cluster refinement and Debye scattering analysis. The resolution function of the setup is also characterized. We conclusively show that high-quality data can be obtained from a single ∼30 fs XFEL pulse for multiple different sample types. Our efforts not only significantly increase the existing maximum reported Q range for an

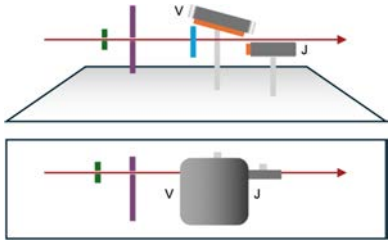

$S(Q)$ measured at an XFEL but also mean that XFELs are now a viable X-ray source for the broad community of people using reciprocal-space total scattering and PDF methods in their research.

1. Introduction

Atomic structure drives the properties that give materials their functionality. It is now widely recognized that understanding a material's properties often requires characterizing both its average, long-range structure, and its local structure present over a much shorter range. This is especially clear in materials lacking long-range order, such as liquids and glasses, but is also the case in materials with ostensibly well ordered periodic structures; deviations from the average structure locally can drive key physical behaviours (Keen & Goodwin, 2015; Simonov & Goodwin, 2020). Therefore, whether or not long-range order is present, the ability to study local atomic structure significantly benefits our understanding of a material's overall atomic architecture.

Total scattering, which encompasses both Bragg and diffuse scattering, along with its Fourier transform – the pair distribution function (PDF) – have been instrumental in the study of local atomic structure. Initially mainly applied to the study of liquids and glasses, these techniques were 'rediscovered' many years later for uncovering disorder within crystalline structures (Keen, 2020). Since then, total scattering and PDF analyses have been applied to a wide range of materials, primarily in equilibrium, including crystalline, nanocrystalline, amorphous and liquid systems. The strength of these techniques lies in their universality, enabling the elucidation of atomic structure beyond the constraints of average structural analysis.

The PDF is a weighted probability of finding atom pairs at specific distances (Egami & Billinge, 2003). Key structural properties can be extracted directly from this function: peak positions provide information about local bonding, peak areas provide information about coordination numbers, and peak widths reflect static and/or dynamic atomic disorder. The complexity of the atomic structure in modern functional materials is often reflected in the PDF as a series of overlapping peaks, making it increasingly difficult to interpret the data directly. As a result, model-based approaches are commonly used to derive meaningful structural insights from the PDF. Large-scale 'big-box' techniques sample ensembles of atoms which represent the material's structure (Tucker *et al.*, 2007), whereas 'small-box' techniques focus on interpreting the PDF within the framework of a crystallographic unit cell – an approach often referred to as 'real-space' Rietveld refinement (Farrow *et al.*, 2007). Regardless of the analysis method, obtaining high-quality total scattering data is essential for rigorous structural insights. A critical factor in data quality in total scattering experiments is measuring scattering to high momentum transfer (Q, where $Q = 4\pi\sin\theta/\lambda$) with sufficient signal-to-noise. The maximum Q value (Q_{max}) in reciprocal space directly determines the resolution of the PDF in real space (Egami & Billinge, 2003). Additionally, during the generation of the PDF, the total scattering data are multiplied by Q before performing the Fourier transform, which amplifies noise in the high-Q region. Therefore, achieving high-Q measurements with excellent signal-to-noise is essential for producing high-quality PDFs. Equally important is measuring the data in a manner that enables quantitative normalization of the total scattering; stable detection systems, careful background measurements and calculations of contributions to the experimental data (Compton scattering, absorption, multiple scattering *etc.*) must also be employed (Soper & Barney, 2011).

In recent years, there has been growing interest in studying the process of (dis)ordering itself, including phenomena such as amorphization, crystallization, nanoparticle formation and responses to ultra-fast external stimuli (Terban & Billinge, 2022; Christiansen *et al.*, 2020; Proffen, 2006). These investigations demand not only the high real-space resolution determined by Q_{max} but also the ability to capture temporal changes, with timescales ranging from several hours to femtoseconds. Some of the fastest changes happen in key technologies, from quantum materials and ultra-fast memory to photovoltaics and spintronics (Yasuda *et al.*, 2024; Jiang *et al.*, 2024; Afanasiev & Kimel, 2023; Guo *et al.*, 2024). Many transformative phenomena in materials science – such as photoinduced phase transitions, non-thermal melting, resistive switching and ultra-fast demagnetization – unfold on femtosecond to picosecond timescales (Schmid *et al.*, 2024; Rousse *et al.*, 2001; Bigot *et al.*, 2009; Pan *et al.*, 2022; Weißenhofer & Oppeneer, 2024). Capturing these events in real time requires tools capable of probing atomic positions and electronic configurations with temporal resolution that matches the time over which these nonequilibrium states exist. These 'fleeting moments' might govern key functional behaviour, such as light–matter interactions in perovskites or reveal switching mechanisms in phase-change memory materials, or are the only time that highly transient phases exist during shock-wave compression experiments.

Synchrotron-based diffractometers, with their high X-ray energy and brilliance, are the instruments of choice for X-ray total scattering measurements. They routinely achieve Q_{max} values of around 25 Å^{-1}, enabling high real-space resolution. However, synchrotron measurements typically take a few minutes. Recent advancements have further reduced measurement durations, with high-quality data obtainable in seconds. In some cases, sub-second data acquisition has been achieved, with time resolutions as short as 3 ms (Magnard *et al.*, 2023); however, such measurements are not common, and typical measurement times are still on the order of seconds to minutes. Currently, although synchrotrons are the best source for X-ray total scattering, offering an optimal balance between exceptional real-space resolution and good temporal resolution, they cannot provide the ultra-fast capabilities argued for in the previous paragraph.

XFELs are the pinnacle of modern X-ray sources. Building on concepts developed in the 1970s, XFELs use self-amplified spontaneous emission within a long undulator to generate an exceptionally brilliant and coherent X-ray laser beam from

high-energy electrons (Georgescu, 2020). These facilities offer unparalleled brilliance and temporal resolution. The first XFEL, the Linac Coherent Light Source (LCLS) in the United States, became operational in 2009 (Emma *et al.*, 2010). Since then, five additional XFEL facilities have been established in Japan (Ishikawa *et al.*, 2012), South Korea (Kang *et al.*, 2017), Germany (Decking *et al.*, 2020), Switzerland (Prat *et al.*, 2020) and China (Liu, 2022). The European XFEL began operations in Hamburg, Germany, in 2017 (Tschentscher *et al.*, 2017). It accelerates electrons over a 1.7 km path, achieving energies of over 17.5 GeV. The facility also boasts a high repetition rate of 27000 pulses s^{-1}, with individual pulse durations shorter than 100 fs.

XFELs have opened new frontiers in physics, particularly matter under extreme conditions and materials chemistry, by enabling 'molecular movies' that capture atomic movements with extraordinary temporal precision. Current XFEL setups have excelled in femtosecond serial crystallography and pump–probe experiments, primarily focusing on Bragg diffraction, alongside coherent diffraction imaging and spectroscopy (Støckler, Krause *et al.*, 2023; Nakano *et al.*, 2017; Obara *et al.*, 2017). Total scattering measurements with PDF analysis were first demonstrated at XFELs in the 2000s. One early pump–probe study of gold trimer formation in solution achieved $Q_{max} \approx 6.5$ Å^{-1} for difference structure factors $\Delta S(Q)$ [*i.e.* $S(Q)$ post-pumping minus $S(Q)$ pre-pumping] using an X-ray energy of 15 keV (Kim *et al.*, 2015). Though this was a technological milestone, the spatial resolution of such data was comparable to that achieved with X-ray diffractometers from 100 years ago. Since then, progress to improve the real-space resolution has been limited with Q_{max} values of 7 Å^{-1} and, at best, ∼9 Å^{-1} reported for total scattering structure factors, $S(Q)$, for shock compression measurements [see recent studies using 18 keV X-rays of liquid carbon (Kraus *et al.*, 2025) and liquid tin (Gorman *et al.*, 2024), respectively] or $Q_{max} \approx 8$ Å^{-1} from liquid-jet nanoparticle suspensions in Støckler, Christensen *et al.* (2023). This results from low X-ray energies compounded by difficulties in normalizing data from taxing experimental setups with limited Q_{max}. To the best of our knowledge, the current Q_{max} record for the more straightforward difference structure factor, $\Delta S(Q)$, at an XFEL is 12.6 Å^{-1} (corresponding to a real-space resolution of ∼0.25 Å) (Griffiths *et al.*, 2024). Though this resolution is adequate for simple structural transitions, it remains insufficient for many advanced studies and falls short of what Mo or Ag source diffractometers can achieve. To fully leverage the temporal capabilities of XFELs for total scattering applications, it is essential to improve the real-space resolution of any potential PDF instrumentation. Achieving this goal involves addressing three key challenges: arranging detectors to mitigate the lower-than-ideal X-ray energies of XFELs, improving the experimental environment to reduce backgrounds and designing the experimental protocols to maximize the efficiency of the measurements.

This work presents our efforts to achieve high-quality, ultrafast total scattering and PDF data at the High Energy Density (HED) scientific instrument at the European XFEL. Here, we describe the experimental setup in detail, including the use of a tilted detector geometry designed to maximize counting statistics in the high-Q region. Additionally, we outline the data processing and reduction pipeline, ensuring precision and efficiency. To demonstrate the versatility of this setup, we present measurements across a diverse range of materials applications, highlighting its broad utility and potential for using these methods at XFELs for groundbreaking insights.

2. Methods

2.1. Experimental setup

Our experiments used the HED scientific instrument at the European XFEL in Hamburg. The experiments were carried out in interaction chamber one (IC1), which operates under a $< 10^{-4}$ mbar vacuum, thus eliminating background contributions from air scattering. General details about IC1 and HED are given in Zastrau *et al.* (2021). We used a Varex 4343CT detector (housed inside a vacuum-tight air pocket with a 400 µm-thick Al window in front of the active face of the detector) and a JUNGFRAU detector (Zastrau *et al.*, 2021), placed to maximize the 2θ coverage and providing the Q range ≈ 0.35–16.6 Å^{-1} with an incident X-ray energy of 24.075 keV and beam energy of ∼150 µJ [Fig. 1(*a*)]. The maximum Q results in an approximate real-space resolution of 0.19 Å. The energy bandwidth was estimated at around 50 eV. Beryllium compound refractive lenses installed 114 m upstream of the target chamber centre (or sample position) of IC1 provided a focused 17 µm (vertical) by 55 µm (horizontal) X-ray beam of low divergence on the sample. The beam size was determined using round edge scans; the vertical dimension is likely to be close to the true beam size of a single pulse, whereas the larger horizontal value reflects the greater beam jitter in this direction and/or an imperfectly adjusted beam bender component. The beam size was selected to be compatible with other instrumentation in the setup; specifically, it was chosen to be smaller than the optical pump laser beams envisaged for future experiments. We also added a set of four tungsten-blade clean-up slits (200 µm × 200 µm) and a stainless steel plate with pinhole upstream of the sample holder to reduce background scattering (Fig. S1 of the supporting information).

The Varex 4343CT detector has a 2880 × 2880 array of 150 µm square pixels and is capable of operating at 10 Hz, the pulse train frequency of the European XFEL. It was placed above the straight-through beam at an angle of ∼15° to the horizontal, covering $9° \lesssim 2\theta \lesssim 89°$ in the vertical plane. With this tilted detector arrangement, which follows the work described in Burns *et al.* (2023), the position of nearest incidence of the detector is 171 mm from the sample at $2\theta \approx 75°$. The main advantages of this detector arrangement are threefold. Firstly, the detector is closest to the sample at higher scattering angles such that the detector solid angle is maximized where the sample scattering is weakest. Secondly, the detector is further from the sample at low 2θ, increasing the

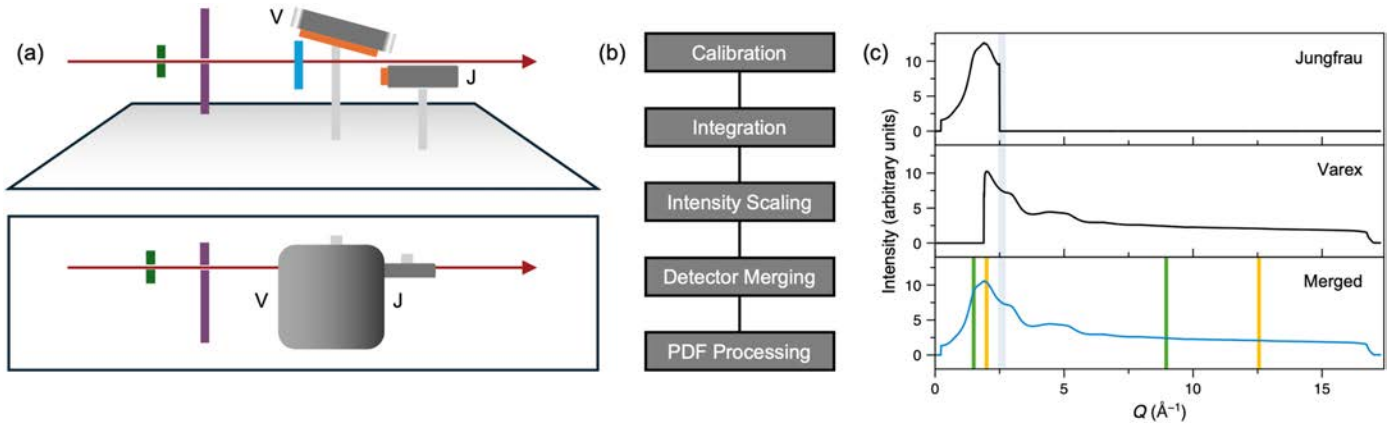

Figure 1
(*a*) Schematic of the main diffractometer components (upper: side view, lower: plan view). The X-rays (red) emerge from the standard HED IC1 components and pass into the IC1 vacuum chamber. They then pass through the clean-up slits (green), steel shield (purple), sample in a vertical holder (blue) and below the Varex (labelled 'V') and above the JUNGFRAU (labelled 'J') detectors (active areas in orange) before exiting the IC1 chamber. The Varex detector is not centred above the X-ray beam because of space constraints. The technical drawing of the setup can be found in Fig. S1. (*b*) Outline of the data-reduction pipeline. (*c*) Example of processed data from the two detectors and the fully merged data, using water in a fused silica capillary as an example. [The normalized $S(Q)$ for water from these data is shown in Fig. 10.] Recent Q_{min} and Q_{max} values for XFEL measurements of $S(Q)$ and $\Delta S(Q)$ are shown as green (Gorman *et al.*, 2024) and yellow (Griffiths *et al.*, 2024) vertical lines, respectively. The region over which merging is performed is shaded in grey; data at Q values above and below this shaded region were not used for the JUNGFRAU and Varex detectors, respectively.

detector's resolution for the low-angle Bragg peaks and reducing the likelihood of detector saturation. Thirdly, the range of scattering angles covered is significantly larger than if the detector was placed in the standard manner perpendicular to the X-ray beam. On account of the Varex detector's 16-bit ADC readout, for certain strongly scattering samples, we needed upstream attenuation of the primary beam in order to avoid saturation.

The JUNGFRAU detector is a smaller 2D detector with a 1024 × 512 array of 75 µm square pixels. It has an automatic gain switching feature for each pixel, which allows it to detect single photon events up to high signal levels by gain switching to cover a broad range of count rates (Redford *et al.*, 2018, 2020). The detector is also in an air pocket to operate in vacuum environments (Zastrau *et al.*, 2021). It was placed below the straight-through beam 407 mm behind the sample and at an angle of ∼90° to the horizontal, covering $1^\circ \lesssim 2\theta \lesssim 14.5^\circ$ in the vertical plane. This detector was added to provide data in the low-Q region since the minimum Q possible with the Varex detector inside its vacuum pocket was ∼2 Å^{-1}.

The HED sample scanner accommodates EUCALL (Appleby *et al.*, 2017; Prencipe *et al.*, 2017) standard sample holders, which consist of an outer and inner frame. The inner frame is compatible with variable target mount plates, which are required for flat sample plates or capillaries, the latter of lengths ∼40 mm and ∼70 mm. Capillaries were glued or taped directly to the sub-frames, enabling various diameter capillaries to be used and allowing for flexible sample mounting options. The sample scanner was mounted vertically (Fig. S2), and the accessible area on the sample plate was 100 mm × 100 mm, even with the top edge of the Varex detector air pocket sitting above the sample scanner. The focal point of a camera coincident with the beam was used to place the samples at the target centre of IC1.

3. Data processing

3.1. Overview

We developed a robust data-reduction pipeline to achieve high-quality data suitable for PDF analysis. This process involved the following steps [as represented in Fig. 1(*b*)] and explained in more detail in the sections below. We applied this process to both the mean of selected pulse trains within a run and to those pulse trains individually. Note that for the majority of the experiments, each train only contained a single pulse, which matches the maximum readout time of the Varex detector.

(1) Azimuthal integration of the data from the individual detectors to yield the intensity as a function of Q, $I_x(Q)$.

(2) Scaling and merging of the individual $I_x(Q)$ to form a merged $I_{merged}(Q)$.

(3) Subtraction of background and Fourier transform to calculate the PDF.

3.2. Calibration

Detector calibration was performed using *pyFAI*, specifically using the *pyfai-calib2* tool (Ashiotis *et al.*, 2015). A thin layer of NIST CeO_2 SRM 674b powder sandwiched between two Kapton films was used as the calibrant for both detectors to reduce sample thickness effects. The primary beam energy in the calibration fitting was set to 24.075 keV (a wavelength of 0.51499 Å), and both the energy and the inclination angle of the detector around the incident beam direction were not allowed to refine – the latter to ensure the correct polarization correction was applied.

3.3. Integration

The azimuthal integration of the two detectors was performed using *pyFAI* to convert from a matched pair of

images to a pair of $I_x(Q)$. For both detectors, we determined our own bad pixel masks using a combination of algorithmic and manual processes and applied a correction to account for the effective sensor thickness. In both cases, we also normalized each pixel to absolute solid angle before integration to simplify the combination of the signals from the two detectors. Additionally, we normalized each dataset to the measured intensity on a diagnostic silicon diode upstream of the sample to account for pulse-to-pulse variation in intensity. In cases where primary beam attenuation above 90% was utilized (see above), the diode signal was too weak to be used as a reliable intensity normalization, and so no normalization was used.

The Varex detector exhibits some features which require additional corrections. After subtraction of the signal arising from the dark current in the detector (the 'dark image'), we also applied intensity corrections to account for the attenuation caused by the aluminium window and the detector response, *i.e.* a flat field correction. Data from the JUNGFRAU detector were also corrected for the aluminium window. Details of how these corrections were performed can be found in Fig. S3.

3.4. Merging

To combine the Varex $I_V(Q)$ and JUNGFRAU $I_J(Q)$ data, we first scale $I_J(Q)$ to minimize the difference between $I_J(Q)$ and $I_V(Q)$ in the region where the two overlap (between 1.89 and 2.49 Å^{-1}), applying both an offset and a scale factor *via* a least-squares minimization [Fig. 1(*c*)]. This step is required because of the different sensor efficiencies of the two detectors. Once on the same scale, a smooth Q-dependent weighting scheme was applied using an error-function-based ramp. The error function, centred at Q = 2.2 Å^{-1} and with a width of 0.1 Å^{-1}, scales the overlapping regions of the two detectors. Overlapping intensities were merged, and normalization/count statistics were recomputed accordingly.

3.5. Monitoring of the dark image validity

In the knowledge that the signal arising from the dark current in the Varex (the 'dark image') is time varying and very sensitive to temperature, in each sample run, we pre-checked the applicability of the stored dark image. We did this by collecting a number of frames without accepting X-rays into the interaction chamber and asserting that, after subtraction of the current dark image, the mean intensity should be zero and that the standard deviation of the intensities should be below a threshold of 15 (Fig. 2).

3.6. Correction for sample offset

A sample offset correction was applied by deriving the general expression for a flat-plate detector inclined at an angle α to the incident beam [see equation (1)] for small offsets. Note that in the case of $\alpha = 90°$, the correction simplifies to the expression derived by Hulbert & Kriven (2023). δ is the 2θ offset, S is sample displacement along the beam, R is the sample-to-detector distance and α (here ~15°) is the inclination angle of the detector to the incident beam:

$$\delta = \frac{S\sin(2\theta)\sin(2\theta+\alpha)}{(R-S)\sin(\alpha)+S\cos(2\theta)\sin(2\theta+\alpha)}. \quad (1)$$

3.7. Calculating the total scattering structure factor and pair distribution function

Following the data-processing steps, PDFs were generated from the total scattering *via* normalization and Fourier transformation using either *GudrunX* (Soper, 2011) or *PDFgetX3* (Juhás *et al.*, 2013), following standard procedures. In *GudrunX*, the raw total scattering data were corrected for background, multiple scattering, container scattering and Compton scattering, and for fluorescence and absorption effects (Soper, 2011). In *PDFgetX3*, where the data are corrected using an *ad hoc* approach, the following parameters

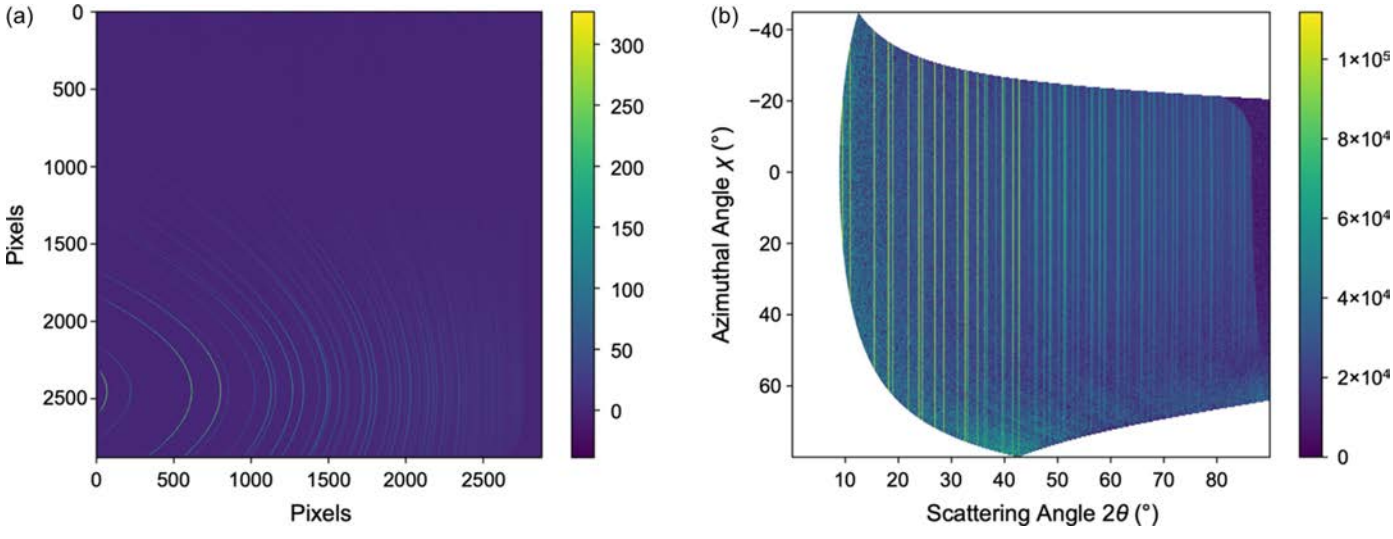

Figure 2
Varex detector images from CeO_2 powdered sample. (*a*) Detector image and (*b*) data plotted as a function of scattering and azimuthal angles, showing vertical lines of intensity corresponding to Bragg reflections. See Fig. S4 for the equivalent data from the low-angle JUNGFRAU detector.

were used: Q_{min}: 0.9–2.2 Å^{-1}, Q_{max}: 15–16.6 Å^{-1}, $Q_{max,inst}$: 16–16.6 Å^{-1}, r_{poly}: 0.9–1.86 (Juhás *et al.*, 2013).

3.8. Sample preparation

Si, CeO_2 and LaB_6 were obtained as certified standard reference materials (SRMs) from the US National Institute of Standards and Technology (NIST). Titanium dioxide P25, silver behenate and ammonium metatungstate were purchased from Sigma Aldrich. The metallic glass ($Fe_{78}B_{13}Si_9$) was purchased from Goodfellow as a 25 µm-thick foil. Silica glass was measured in the form of a fused silica capillary, coated in a thin polyimide layer, with inner and outer diameters of 700 and 850 µm, respectively. All chemicals were used without further purification. Flat-plate samples were prepared by dispersing powders onto Kapton tape. Capillary samples were measured in fused silica (0.7 mm inner diameter) coated with a thin polyimide layer or quartz (0.5 mm inner diameter) capillaries.

4. Results and discussion

We applied our methodology to a diverse set of samples to show that quantitative data over a wide Q range can be obtained across different material types (Fig. 3). We investigated highly crystalline powders (Si, CeO_2, LaB_6 and Ag behenate), a nanocrystalline powder (TiO_2), amorphous solids (silica glass and an $Fe_{78}B_{13}Si_9$ metallic glass), a pure liquid (water) and an atomic cluster in solution (aqueous tungsten Keggin, $[W_{12}O_{40}]^{6-}$).

To determine the diffractometer characteristics, we measured highly crystalline powders using capillary and flat-plate geometries. These were first used to determine the positions of the detectors relative to the sample, and then, because they exhibit minimal sample-induced peak broadening, the instrumental resolution function (IRF).

4.1. Crystalline standards: NIST Si 640b and CeO_2 674

A quartz capillary loaded with NIST Si 640b SRM was measured using a one-pulse-per-train acquisition, averaged over ∼1700 pulses. The resulting diffraction pattern exhibited narrow, symmetric peaks with low background and an excellent signal-to-noise ratio, despite the inclined detector geometry, which places the detector close to the sample and distorts the Debye–Scherrer powder rings. The data spanned a 2θ range of 1.1 to 86.0° (0.23 to 16.6 Å^{-1}). Even at the highest angles, Bragg peaks remained sharp with good signal-to-noise (the latter due to the increasing solid angle with increasing 2θ).

Rietveld refinement using *TOPAS Academic* (Coelho, 2018) yielded a high-quality fit (R_p = 6.392%, R_{Bragg} = 3.045%) and an atomic displacement parameter, B_{iso}(Si), of 0.328 (7) Å^2 using a fixed lattice parameter (certified by NIST) of 5.43094 Å [Fig. S5(*a*)]. The peak shapes were well described using a standard pseudo-Voigt profile, and background modelling was performed using a 13th-order Chebyshev polynomial. The sample offset was determined to be −0.039 (1) mm relative to the nominal diffractometer centre [see equation (1) above].

Following normalization, the NIST Si 640b reciprocal-space data were Fourier transformed into a PDF using *PDFgetX3* (Juhás *et al.*, 2013) and the Q range 1.7 to 16 Å^{-1}. The resulting PDF displayed sharp peaks with minimal damping at high r, confirming negligible instrumental contributions. Small-box Rietveld refinement in *PDFgui* (Farrow *et al.*, 2007) produced a good fit (R_p = 13.7%), a lattice parameter of 5.4316 (7) Å and a B_{iso}(Si) of 0.5 (1) Å^2 [Fig. S5(*b*)]. The instrumental parameters, Q_{damp} and Q_{broad}, were determined to be 0.006 (4) and 0.009 (4), respectively. The difference curve had some oscillatory behaviour, possibly an artefact from the Fourier transform of the merged region of the data (which occurs in the region between 1.89 and 2.49 Å^{-1}). A joint refinement of powder diffraction and PDF data in *TOPAS Academic* (Coelho, 2018) yielded similar results (R_w = 6.72%), with a B_{iso}(Si) of 0.42 Å^2 – close to the average of the values obtained from refinements using *TOPAS Academic* of the powder diffraction pattern and PDF data separately (Fig. 4).

To assess the feasibility of ultra-fast total scattering measurements, NIST CeO_2 674 SRM powder in a fused silica capillary was measured using a single XFEL pulse (∼30 fs) with only 10% of the full X-ray beam intensity. Remarkably, despite the extremely short acquisition time, around 16 orders of magnitude faster than a typical synchrotron measurement, the diffraction pattern exhibited sharp Bragg peaks and a high signal-to-noise ratio [Fig. 5(*a*)]. Rietveld refinement of the single-pulse data yielded a mean R_p of 8.26 (1.14)%, R_{wp} of 10.85 (1.56)%, a lattice parameter of 5.4079 (0.0018) Å, and B_{iso} (Ce) of 0.25 (0.04) Å^2 and B_{iso} (O) of 0.51 (0.17) Å^2, using a Thomson–Cox–Hastings pseudo-Voigt (TCHZ) peak profile.

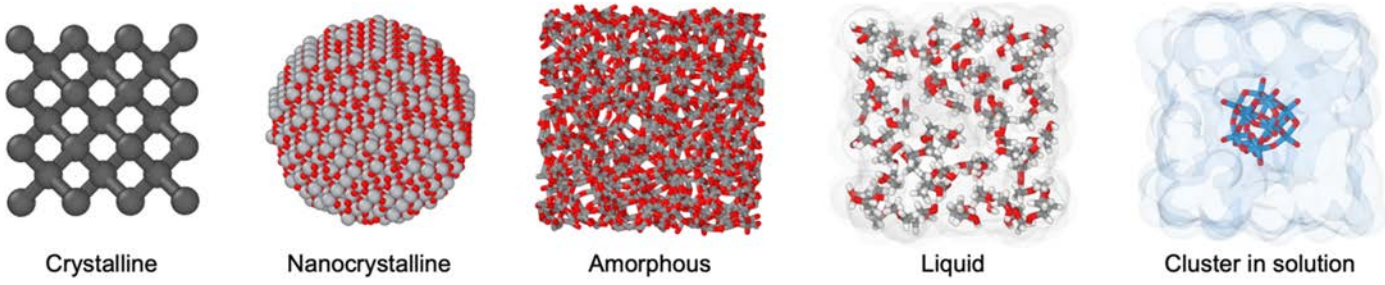

Figure 3
Overview of the material types measured in this study.

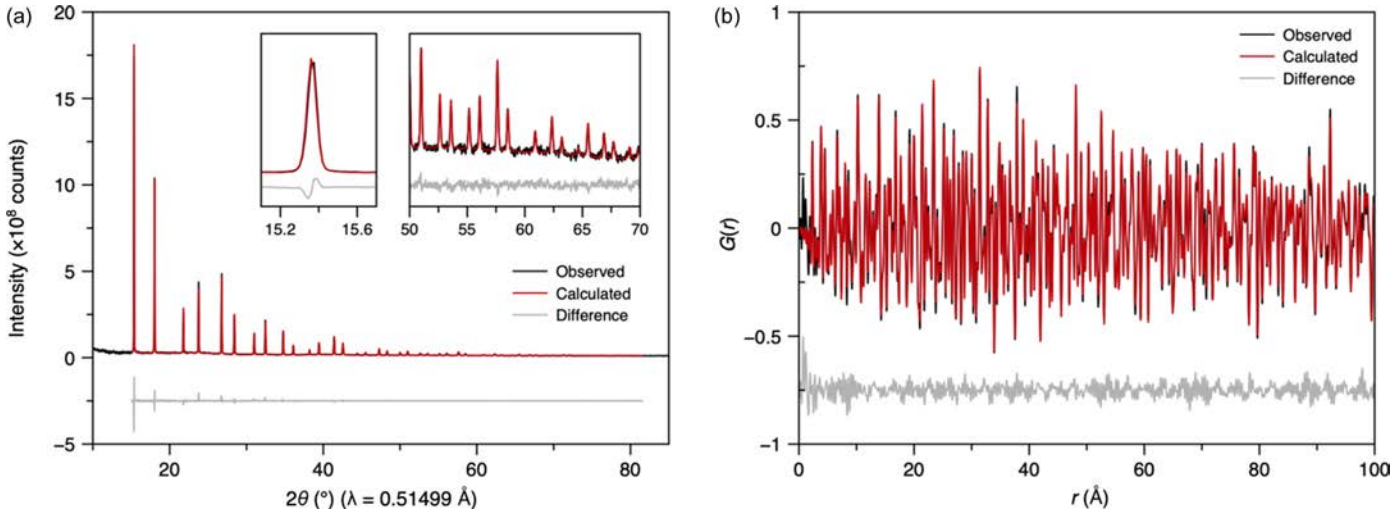

Figure 4
(*a*) Rietveld refinement of averaged normalized powder diffraction data of NIST Si 640b SRM loaded in a quartz capillary. Insets show enlarged regions of the data at low and high 2θ. (*b*) Small-box 'real-space Rietveld' refinement against the PDF obtained from the data in (*a*). The Rietveld and small-box PDF refinements shown in (*a*) and (*b*), respectively, were carried out simultaneously using *TOPAS Academic* software (Coelho, 2018).

Here we give the values' mean and standard deviation (in brackets) obtained from refinements of 74 single-pulse measurements. These values compare reasonably well to previously reported atomic displacement parameters of 0.292 and 0.395 Å^2 for B_{iso} (Ce) and B_{iso} (O), respectively, obtained from synchrotron data (Yashima & Takizawa, 2010).

The CeO_2 single-pulse diffraction data were transformed into PDFs using *PDFgetX3* [Fig. 5(*b*)]. Small-box refinement in *TOPAS Academic* yielded a mean R_p of 18.1 (1.5)%, R_{wp} of 18.2 (1.5)%, a lattice parameter of 5.4078 (0.0017) Å, B_{iso}(Ce) of 0.165 (0.022) and B_{iso}(O) of 1.58 (0.26) Å^2 (mean and standard deviations from the same 74 single-pulse datasets used for the Rietveld refinements given above). These are consistent with previously reported B_{iso} values of 0.226 and 1.55 Å^2 for Ce and O, respectively; however, it is known that the values obtained from Rietveld refinement of the reciprocal-space data are more reliable (Neder & Proffen, 2020). Overlays of multiple single-pulse reciprocal-space data and PDFs revealed little variation between pulses, indicating high reproducibility (Fig. S6).

As expected, averaging multiple single-pulse measurements further improved the signal-to-noise [Figs. 5(*c*) and 5(*d*)]. However, even single-pulse data exhibited low noise, emphasizing the exceptional quality of the setup. Rietveld and small-box refinements using the averaged data closely matched the single-pulse results (Fig. S7). The averaged Rietveld refinement yielded an R_p of 4.846%, lattice parameter of 5.4075 (5) Å, B_{iso} (Ce) of 0.253 (4) Å^2 and B_{iso} (O) of 0.48 (3) Å^2. The lattice parameter was almost identical to those obtained from the single-pulse measurements, emphasizing the high reproducibility of our measurements. Again, these values compare well to previously reported results from synchrotron data (Yashima & Takizawa, 2010). The average small-box refinement yielded an R_p of 16.022%, lattice parameter of 5.40747 (4) Å, B_{iso} (Ce) of 0.165 (3) Å^2 and B_{iso} (O) of 1.53 (2) Å^2.

The IRF was extracted from the averaged CeO_2 data as a function of 2θ (Fig. 6). The variation in FWHM was around 0.03 to 0.25° in the range 10 to 80°. An essentially identical IRF was obtained from LaB_6 (Fig. 6), with the peak broadening in both cases being dominated by instrumental contributions (Fig. S8).

4.2. Crystalline standard for low-*Q* measurements: Ag behenate

To assess performance at low *Q* values, we measured silver behenate, known for its well defined Bragg peaks extending down to $Q \approx 0.15$ Å^{-1} (Blanton *et al.*, 2011). The expected low-*Q* peaks were observed in the JUNGFRAU detector. The Bragg peaks were symmetric and well modelled using the pseudo-Voigt peak shape. A Pawley refinement was successfully carried out using previously reported lattice parameters, confirming the setup's capability to cover both low- and high-*Q* scattering (Fig. 7).

4.3. Nanocrystalline TiO_2 for total scattering analysis using *DebUsSy*

A nanocrystalline TiO_2 P25 powder (with ~25 nm particles) was measured in capillary geometry. The data were averaged, corrected for absorption and the signal from an empty quartz-glass capillary was subtracted (Fig. 8). As expected, the Bragg peaks are broader than those seen in the Si and CeO_2 data due to the crystallite size of the TiO_2 powder. By making use of the IRF, the sample broadening from TiO_2 could then reliably be extracted and analyzed.

The sample contained ~90% anatase and ~10% rutile polymorphs of TiO_2. Reciprocal-space data analysis was performed using the Debye scattering equation [within the *DebUsSy* program suite (Cervellino *et al.*, 2015)] and an atomistic model of nanocrystals similar to that described in Bertolotti *et al.* (2020). The anatase unit cell [refined from

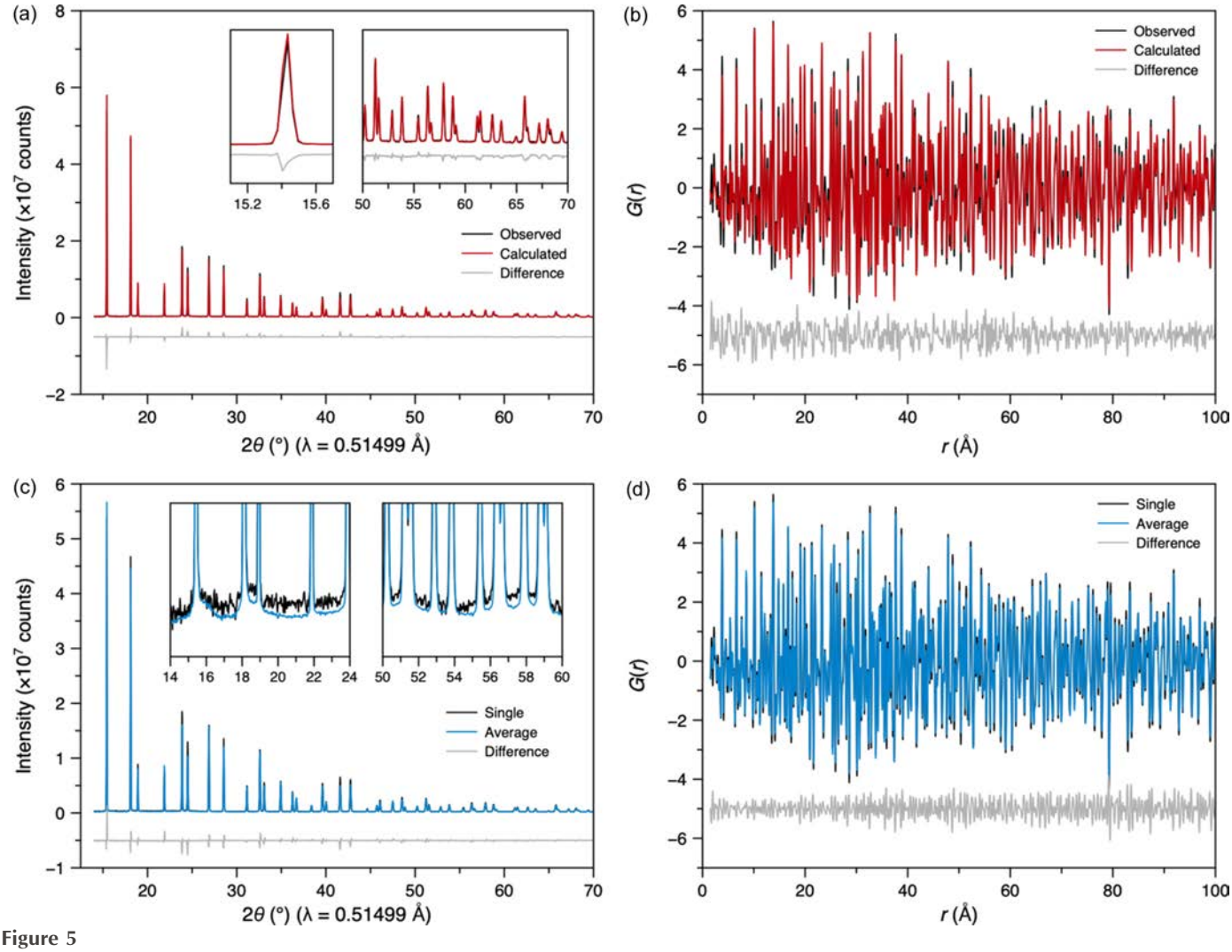

Figure 5
(*a*) Representative Rietveld refinement of normalized powder diffraction data of NIST CeO_2 674 SRM in a fused silica capillary obtained from a single attenuated pulse of XFEL radiation. Insets show enlarged regions of the data at low and high 2θ. (*b*) Small-box 'real-space Rietveld' refinement against the single-pulse PDF obtained from the data in (*a*). (*c*) Comparison between diffraction data from a measurement using a single pulse and that averaged over 74 pulses. Insets show enlarged regions of the data at low and high 2θ. (*d*) PDF data equivalent to the data in (*c*).

synchrotron data $a = b = 3.7860$ Å, $c = 9.5080$ Å (Bertolotti *et al.*, 2020)] was used as a building block to generate a bivariate population of prismatic nanocrystals according to two independent growth directions, one along the *c* axis (L_c) and the other in the *ab* plane (D_{ab}). The minority rutile phase (composed of larger ~50 nm nanocrystals) was modelled as a blank trace using the calculated pattern from *TOPAS* software (Coelho, 2018). A good fit ($R_p = 5.29\%$) was obtained over the range $1.6 < Q < 14.9$ Å^{-1} with B_{iso}(Ti) = 0.20 Å^2 and B_{iso}(O) = 0.35 Å^2. These values are underestimated compared with those extracted from synchrotron data (collected at the X04SA Material Science beamline of the Swiss Light Source). By convoluting the instrumental peak broadening obtained from the IRF previously extracted from LaB_6 in Fig. 6 to the DSE calculated pattern, the sizes and their relative dispersions (σ) of the slightly anisotropic anatase nanocrystals were extracted ($D_{ab} = 23.88$ nm, $\sigma/D_{ab} = 0.37$, $L_c = 17.91$ nm, $\sigma/L_c = 0.41$), described by a discrete bivariate lognormal distribution function. These results are in excellent agreement with the

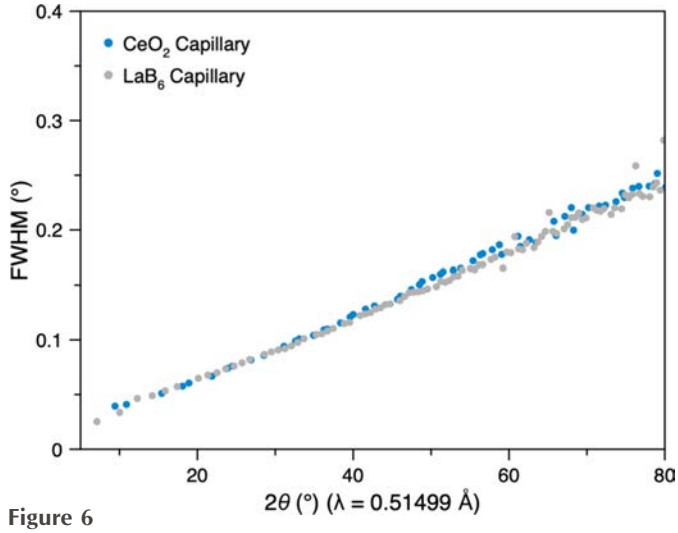

Figure 6
Comparison between the Bragg peak full width at half-maximum (FWHM) obtained from averaged powder diffraction data of CeO_2 and LaB_6 in capillaries, as a function of scattering angle, 2θ.

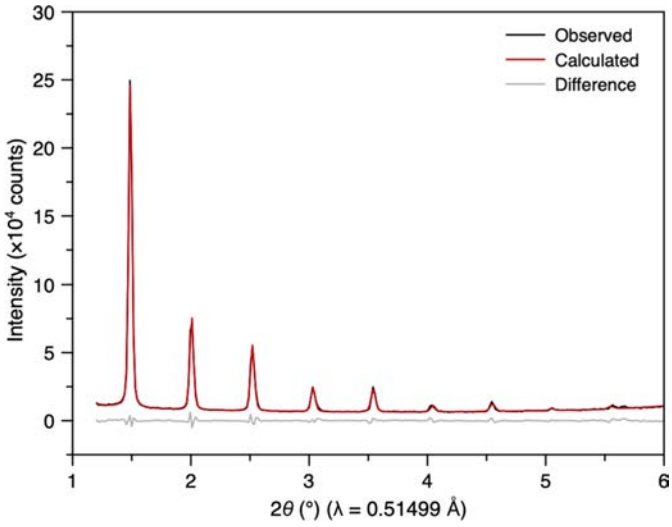

Figure 7
Pawley refinement of silver behenate using averaged powder diffraction data from the low-angle JUNGFRAU detector.

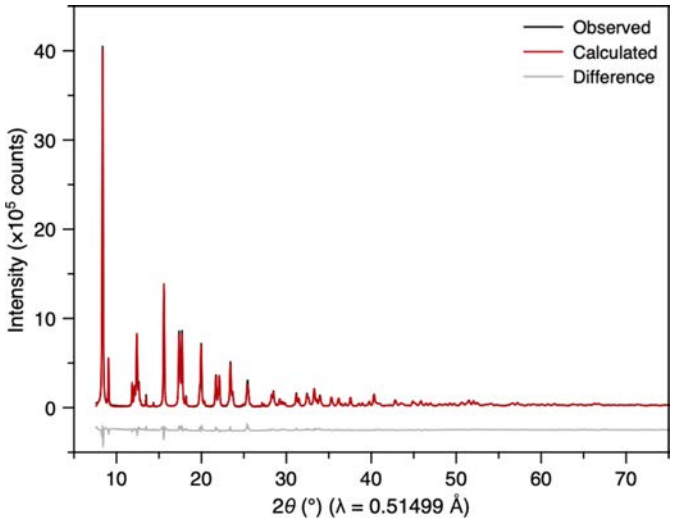

Figure 8
Debye scattering analysis of averaged powder diffraction data from nanocrystalline TiO_2.

previous results obtained from synchrotron data (Bertolotti *et al.*, 2020).

4.4. Total scattering data from amorphous silica and a metallic glass: comparison with synchrotron data

The structures of amorphous materials, lacking long-range order, can only be studied using total scattering/PDF methods and therefore these XFEL developments are especially important for this class of materials. PDFs for the amorphous samples reported here were generated using the *GudrunX* software, since this software produces absolutely normalized total scattering structure factors, $S(Q)$, and PDFs, $D(r)$,[1] that can be directly compared with previously normalized data (Soper, 2011; Keen, 2001). The PDFs presented here are the sine Fourier transforms of $S(Q)$ using Q values between 0.35 and 15 Å^{-1}.

For SiO_2 glass, the so-called first sharp diffraction peak was observed at 1.54 Å^{-1} [Figs. 9(*a*) and S9], consistent with previous reports (*e.g.* Kohara & Suzuya, 2003). The PDF contained the expected peaks corresponding to the SiO_4 tetrahedra in the structure [Fig. 9(*b*)], with peaks at 1.6 (Si—O), 2.6 (O—O) and 3.1 Å (Si—Si). Comparisons with synchrotron data reveal remarkable agreement for the $S(Q)$ over the whole measured Q range and for the PDF [Figs. 9(*a*) and 9(*b*), respectively]. Moreover, there was only a 1.52% variation in the relative Si—O coordination numbers determined from the peak at 1.6 Å. These results highlight the advantage of the combined Varex–JUNGFRAU detector setup, which provides access to the low- and high-Q values necessary for studying amorphous samples.

A metallic glass ($Fe_{78}B_{13}Si_9$) was also measured, with excellent agreement between its $S(Q)$ and PDF and those measured on I15-1 at Diamond Light Source [Figs. 9(*c*) and 9(*d*)]. The most significant deviation between the two datasets is in the lowest-Q region of $S(Q)$, where it is often difficult to get reproducible results between instruments. The first three low-r peaks in the PDF are observed at 2.56, 4.22 and 5.02 Å [Fig. 9(*d*)], most likely corresponding to the nearest, next-nearest and next-next-nearest Fe–Fe distances of an approximately close-packed arrangement of the iron atoms in the glass. Impressively, good quality $S(Q)$ and $D(r)$ data were successfully obtained from just a single XFEL pulse (∼30 fs) (Fig. S10). Additionally, the $S(Q)$ and PDFs generated by *GudrunX* and *PDFgetX3* were very similar (Fig. S10), except for some low-r deviations in the PDF and an overall scale factor, due to the assumptions implicit in *PDFgetX3*'s *ad hoc* approach (Juhás *et al.*, 2013).

4.5. Assessment of liquid and solution diffraction: water and Keggin solution

In addition to amorphous solids, liquids are a critical class of materials studied using total scattering. Water was selected due to the extensive literature on its total scattering and for the challenge of its relatively weak X-ray scattering signal. A well normalized $S(Q)$ was obtained using *GudrunX*, with the key double peak maxima observed at 2.08 and 2.93 Å^{-1} (Fig. 10), closely matching reference data (Soper, 2013). The PDF was generated, exhibiting the characteristic O–O peak present at 2.83 Å (Fig. S11), and was also in agreement with reference data (Soper, 2013).

We then tested the ability to detect atomically precise clusters in solution by studying the tungsten Keggin cluster ($[W_{12}O_{40}]^{6-}$), which forms upon dissolution of ammonium metatungstate in water. A 1.0 M solution (with respect to [W]) was loaded into a fused silica capillary and measured. As expected for a cluster in solution, over 70% of the total scattered intensity originated from the capillary and solvent in the Q range 0.9 to 16.5 Å^{-1} [Fig. 11(*a*)]. Nevertheless, a

[1] Note on correlation functions: to avoid confusion, PDFs produced using *PDFgetX3* or *GudrunX* are labelled '$G(r)$' or '$D(r)$', respectively. The '$G(r)$' function used here is the function '$G^{\rm PDF}(r)$' in Keen (2001), which also describes how '$G^{\rm PDF}(r)$' and '$D(r)$' are related.

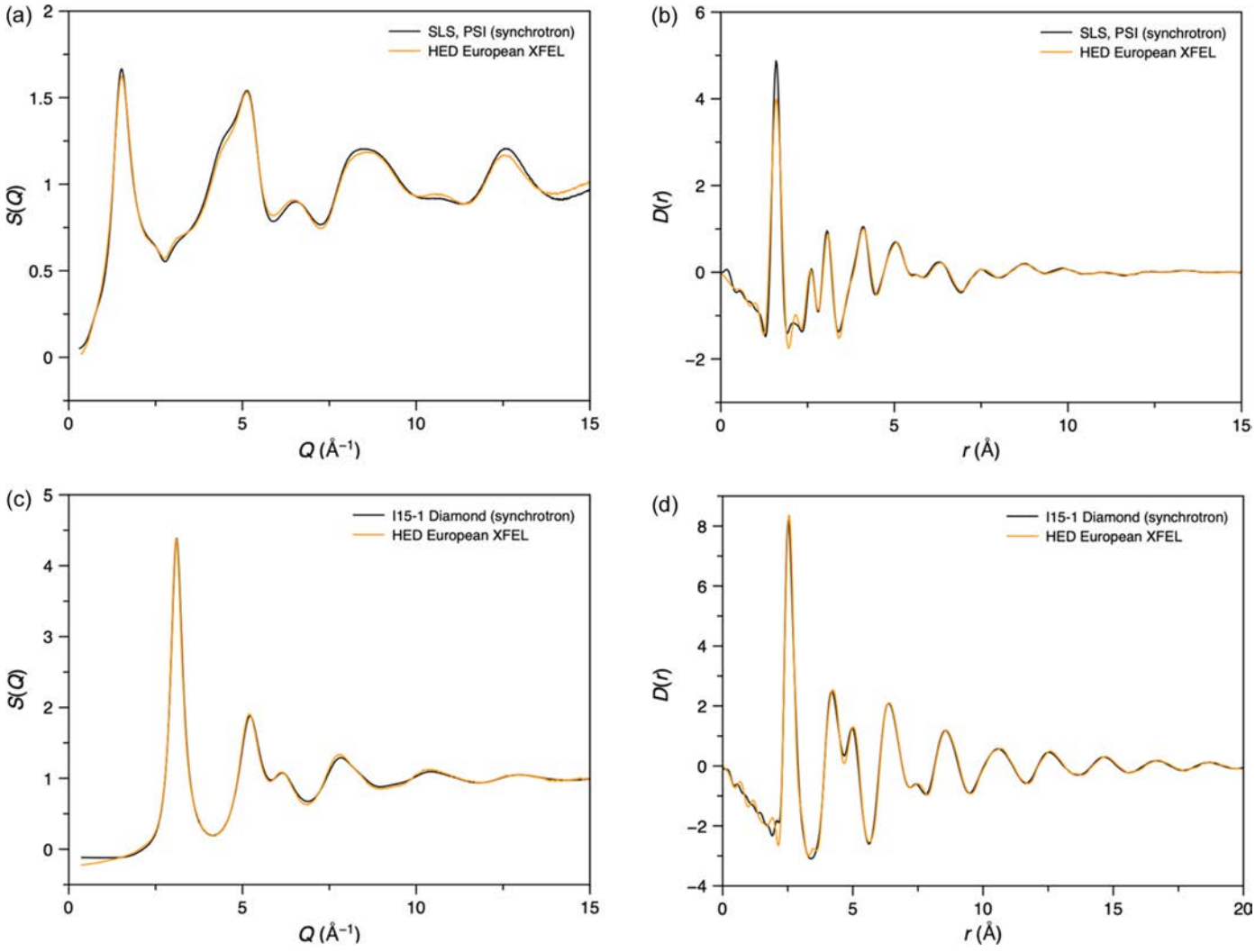

Figure 9
Averaged (*a*) $S(Q)$ and (*b*) PDF data for SiO_2 glass compared with similar synchrotron data (SLS, PSI, Switzerland). Synchrotron data were collected from a 2 mm-diameter silica glass rod using a Mythen II detector and a 28 keV X-ray beam (unpublished data collected by Antonio Cervellino). Averaged (*c*) $S(Q)$ and (*d*) PDF data for a single 25 µm layer of commercial metallic glass, $Fe_{78}B_{13}Si_9$, compared with similar data obtained from four layers of the same glass measured on the I15-1 diffractometer at Diamond Light Source (data measured by Daniel Irving as part of the I15-1 mail-in service, proposal CY39017).

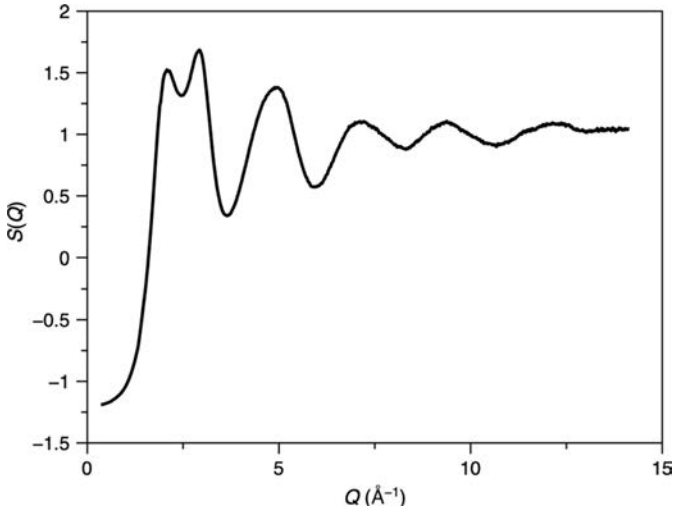

Figure 10
Average $S(Q)$ obtained from water.

distinct signal from the Keggin structure was observed after subtracting the background from the capillary and solvent and was used to generate the PDF [Fig. 11(*b*)]. Key peaks in the PDF were observed at 1.91 Å (W–O) and 3.27 (W–W), 3.72 (W–W) and 6.05 Å (W–W). To further evaluate the sensitivity of the setup, we measured the Keggin cluster across a concentration range from 0.2 to 1.0 M [Fig. S12(*a*)]. Even at the lowest concentration, a clear signal from the cluster was detected, and almost identical PDFs were generated across the range of concentrations.

The structure of the Keggin cluster was then refined against the PDF using cluster modelling within the *DiffPy-CMI* framework [Fig. 11(*b*)] (Juhás *et al.*, 2015). The atomic structure of the Keggin cluster was extracted from the ammonium metatungstate crystal structure (Magnard *et al.*, 2023). The PDF was then calculated from this structure *via* the $I(Q)$ computed from the Debye equation. To refine the model against the data, an overall scale factor, two isotropic thermal

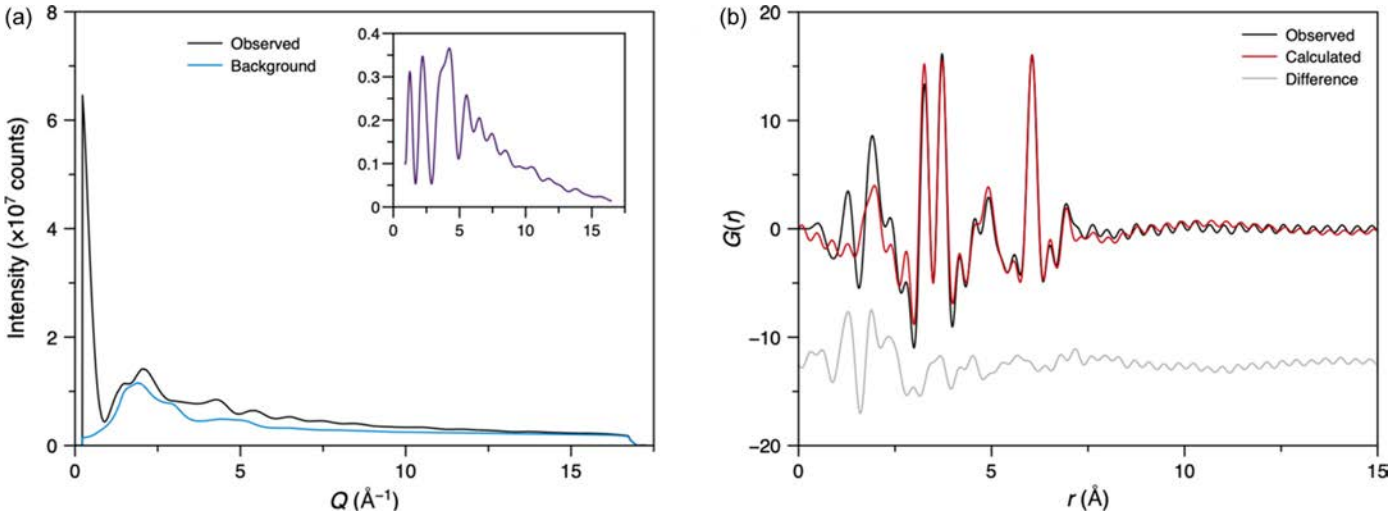

Figure 11
(*a*) Measured average intensity of the fused silica capillary loaded with the aqueous 1.0 M Keggin solution and a capillary loaded with water (background). Inset shows the sample intensity after background correction (omitting the intensity at low Q that most likely is a small-angle X-ray scattering contribution). (*b*) Average PDF of the Keggin cluster in solution and a model refined in *DiffPy-CMI*.

displacement parameters (*i.e.* for W and O), a parameter δ_2 (which accounts for correlated motion effects) and a zoom-scale parameter (which stretches/compresses the atomic structure isotropically whilst maintaining relative atomic positions) were all varied in a similar approach to Magnard *et al.* (2023). A good refinement was obtained (R_w = 33.8%), similar to previous reports (Magnard *et al.*, 2023), with a zoom-scale parameter of almost unity (1.01) and B_{iso}(W) = 0.22 (2) Å^2 and B_{iso}(O) = 0.18 (2) Å^2. Below r = 2.5 Å, the difference function exhibited more significant and structured features; these were identified as contributions from the ammonium cation and its solvent-restructuring effects, which were not accounted for in the model, by comparison to reference data collected at DanMAX, MAX IV (unpublished data collected by Adam Sapnik) [Fig. S12(*b*)].

As a final demonstration of the high-quality nature of the data, the PDF of the Keggin cluster was extracted from an $S(Q)$ of a 1 M Keggin solution measured using only a single XFEL pulse (∼30 fs) over the Q range 0.9 to 16 Å^{-1}. This was then compared with a synchrotron measurement of 5 min from a 2 M solution collected at DanMAX, MAX IV (unpublished data collected by Adam Sapnik) (Fig. 12). Despite more than 70% of the signal arising from background scattering, an increased concentration of the Keggin in the synchrotron measurement, and, most impressively, a 16 order of magnitude reduction in acquisition time, the PDF obtained from HED is of remarkable quality and is very clearly comparable to that obtained using synchrotron radiation. Minor differences in the PDFs are observed below 3 Å, where PDFs are typically less reliable and from differences in the counterion solvation environment with concentration. Beyond 10 Å, no structural signal is present, and the variations here arise from termination effects and the different signal-to-noise statistics of each measurement. Ultimately, this result alone highlights the success of our efforts, demonstrating high-quality ultra-fast PDF on one of our most challenging samples.

5. Conclusions and outlook

Over the past 40 years, total scattering and PDF measurements have become increasingly crucial for determining short-range correlations within all types of condensed matter (crystalline, glass, liquid *etc.*) (Keen, 2020). At the same time, relevant technological topics are increasingly reliant on the behaviour of local structures to understand material functions. Examples of this include ionic conduction in battery materials, local distortions in ferroelectrics, or gas absorption in porous materials. If this is combined with the need to understand glass structure for increasingly 'smart' amorphous materials or the underlying fundamental physics of geologically relevant liquid structures under highly non-ambient conditions, or the nanoscale structure of non-equilibrium metastable quantum

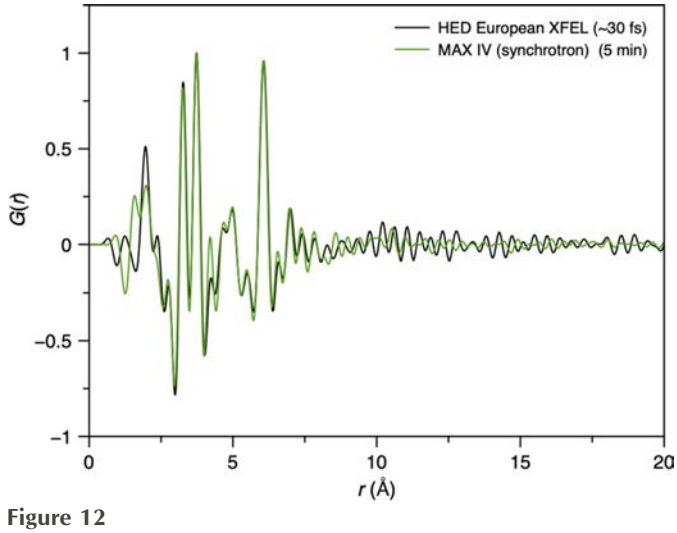

Figure 12
Comparison between a PDF from 1.0 M Keggin solution obtained using a single XFEL pulse (green) and a 5 min synchrotron measurement of a 2.0 M Keggin solution (black).

states exhibiting ultra-fast optical or electrical switching, then it is clear that these techniques will continue to be important for some time to come.

Note that many disordering processes – or the formation of novel nanoscale states – occur on timescales inaccessible to total scattering measurements at conventional synchrotron sources. These ultra-fast dynamics can only be captured through carefully designed experiments at XFEL facilities, where the combination of femtosecond pulses and high photon energies provides unique access to this regime. Such measurements inherently require meticulous preparation and precision but are essential for probing processes that are far too rapid for even the most advanced synchrotron techniques. The outlook is highly promising – strengthened by the results presented in this work and the continued advancement toward higher-energy X-rays at XFEL facilities. We are confident that total scattering and PDF measurements at XFELs will steadily improve, offering increasingly profound insights into the structural dynamics of complex materials.

We have shown that quantitative total scattering data can be obtained from carefully designed XFEL instrumentation over a wide range of Q values, achieving a Q_{max} above 16 Å^{-1} whilst simultaneously measuring data down to a Q_{min} of 0.35 Å^{-1}. This maximum Q is nearly twice what is currently routine and a third higher than has been achieved for the less stringent $\Delta S(Q)$ measurements often used for pump–probe experiments. The data are now sufficient to produce PDFs with reasonable real-space resolution for quantitative studies of disordering structural processes. We have also shown that higher Q_{max} are possible – to values approaching 20 Å^{-1} (see Figs. 13–16 in Appendix *A*) – but these are currently only possible by collecting data at scattering angles above $2\theta = 90°$ which starts to negate the benefits of the angled Varex detector and compromises the versatility of having sample mounting systems perpendicular to the incident X-ray beam. Routine total scattering measurements with Q_{max} greater than 16 Å^{-1} will, therefore, probably only be realistic following XFEL source upgrades that provide higher-energy X-ray beams.

The key result of this work is that high-quality, quantitative total scattering and PDFs have been obtained from single ∼30 fs X-ray pulses. We have demonstrated this using a range of samples with a wide variety of structure types, all of which have produced data of similar quality to that available at synchrotron sources over the range of Q that we have measured. The experiments have been carried out on the HED instrument at the European XFEL, but the specific apparatus needed for the measurements (Varex detector, background-reducing components *etc.*) is readily available and could be installed at other high-energy XFEL instruments. We have also developed data-analysis pipelines to simplify the data collection and normalization process, and we have shown that these produce data suitable for most of the data normalization and analysis tools currently in use by the community.

We are confident that this work will pave the way for new time-resolved studies in catalysis, battery materials, phase transitions, nanoparticle nucleation, nanoscale structure characterization of hidden non-equilibrium states and any area of science where time-resolved total scattering or PDFs will be of benefit. Hence, the next obvious step is to link these measurements to pump–probe techniques where delays of tens of femtoseconds and longer can be used to study, for example, optical-electronic-phononic induced changes. In this regard, the positioning of the detectors is helpful because they do not obscure the horizontal plane or substantially obscure the vertical plane perpendicular to the X-ray beam, both of which pass through the sample position. Hence pump and diagnostic lasers can be used in their typical (*i.e.* horizontal) arrangements, as well as vertical applied fields and liquid-jet sample delivery systems. The quality of PDF data available from solutions shows that we have an important tool for studies of rapid conformational changes in molecules in solution. The measurements are also highly relevant for those studying high-pressure, high-temperature liquids produced by shock waves. The high-pressure shock wave community is strong, and the quality of the total scattering data now available means that measurements of more complex compounds, where higher-resolution data are essential, are now tractable.

APPENDIX *A*

Summary of HED experiment using four JUNGFRAU detectors around the sample

Our initial aim was to collect data to a maximum $Q \approx 20$ Å^{-1}. To do this, we placed four JUNGFRAU detectors around the sample position in IC1 of HED in the vertical plane (see Fig. 13). The three within the vacuum chamber were above the horizontal and extended to a scattering angle of ∼110°. There was also a detector outside the vacuum chamber of IC1 (see Fig. 13) that was below the horizontal and covered some of the low-2θ angles not accessible to the lowest JUNGFRAU within the IC1 vacuum chamber. This arrangement gave a Q_{max} of 19.9 Å^{-1} but at the expense of gaps in 2θ coverage where there were no detectors. In order to provide access to these higher scattering angles, the sample stage was mounted at 120° to the horizontal (*i.e.* the normal to the plane of the stage pointed to a 2θ of 30°).

Limitations on space and geometry meant that the Q range was not continuous [see Fig. 14(*a*)]. We explored several options for interpolating the missing data between detectors with some success. For crystalline samples, where the Bragg scattering is orders of magnitude greater than the diffuse scattering, robust interpolation routines could be developed with little impact on the PDF [see Figs. 14(*b*) and Figs. 15(*a*)]. For samples where the signal is dominated by diffuse scattering, interpolation proved more challenging and severely impacted the PDF, giving rise to various artefacts. Furthermore, the data at high Q were fairly weak due to a low solid angle coverage in this region. Given our aim of establishing high-quality total scattering that is reliable, reproducible and robust for highly crystalline materials and a broad cross section of materials (including liquids and glasses), we chose

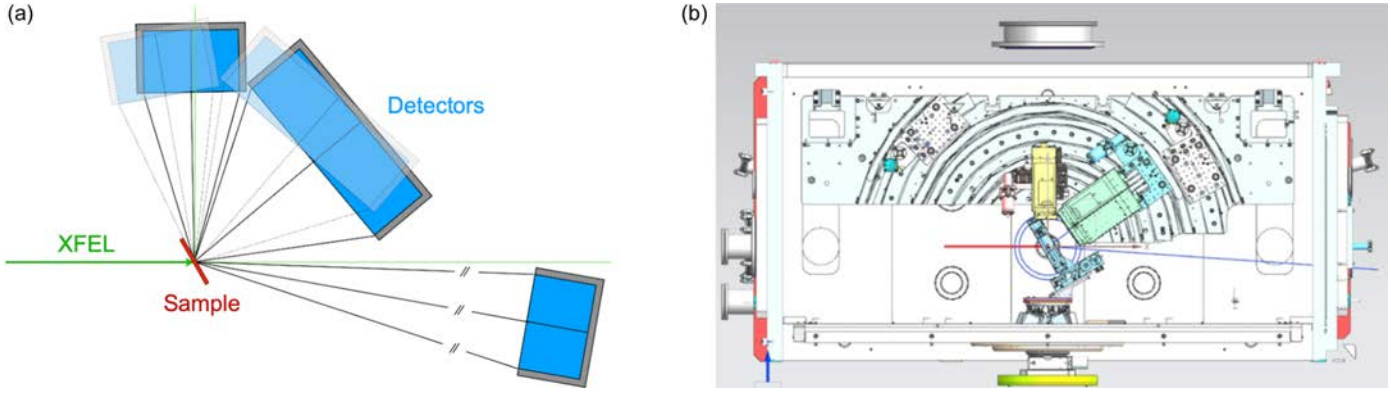

Figure 13
(*a*) Schematic and (*b*) CAD drawing of the detector arrangement using four JUNGFRAU detectors. The fourth detector placed below the X-ray beam outside the IC1 vacuum vessel is not shown in (*b*), and the three highest-angle detectors were mounted on movable arms, although in practice they were not rotated.

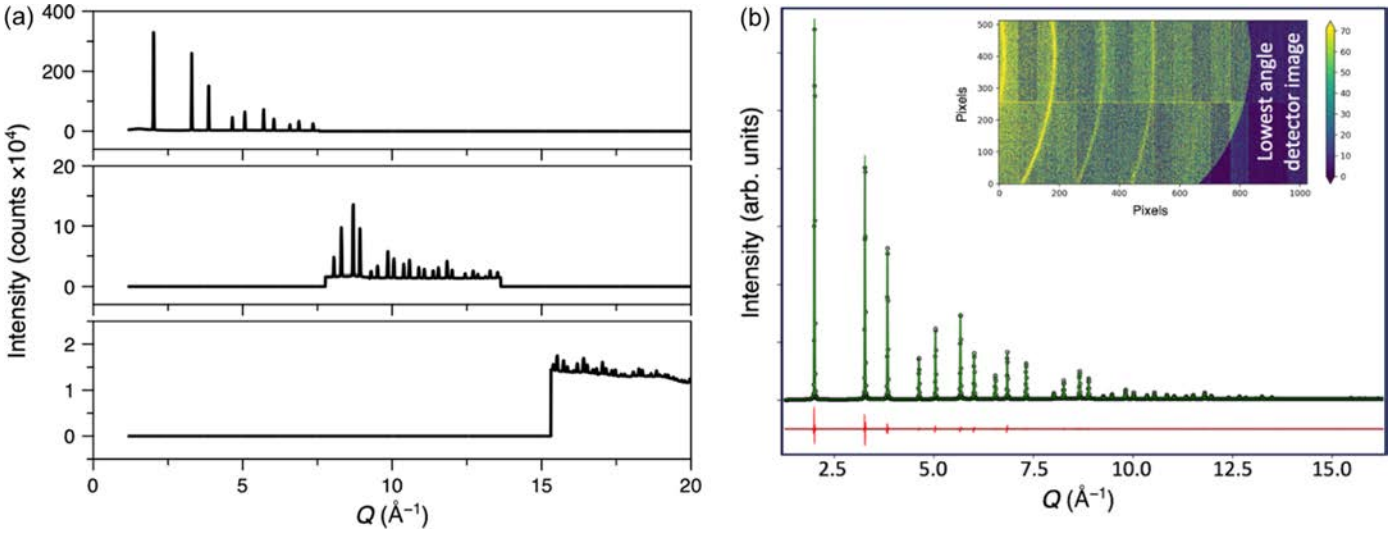

Figure 14
Integrated data from a NIST Si 640b sample from the three highest-angle detectors shown (*a*) separately and (*b*) merged into a single diffraction pattern (points). (*b*) also shows a Rietveld refinement (green line), difference (red line, offset) and a 2D image of the data in the fourth (lowest angle) detector of Ag behenate showing its characteristic low-*Q* powder lines (inset).

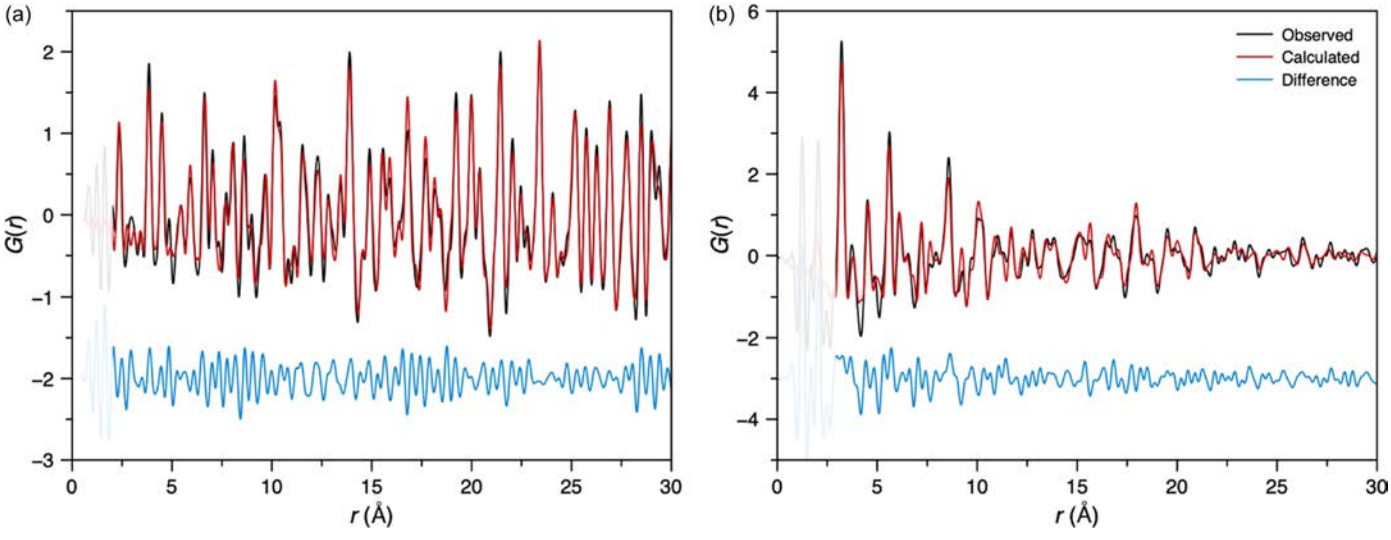

Figure 15
(*a*) Small-box refinement of NIST silicon 640b using average PDF data. (*b*) Refinement of ZnO nanoparticles against a PDF obtained from a single pulse.

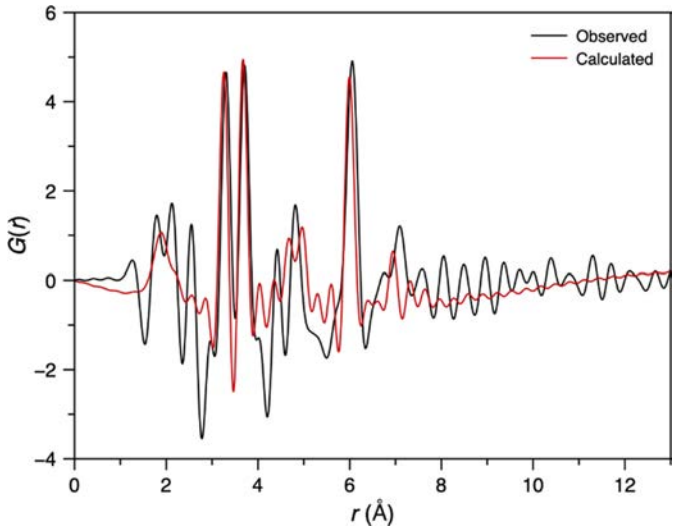

Figure 16
Comparison between the experimental and calculated PDFs from the Keggin cluster in water.

to pursue the Varex detector setup described in the main text instead.

Nonetheless, the PDFs that we extracted from some standard materials (see Figs. 15 and 16) were reasonably robust and could be fitted with the calculated functions based on their published structures.

Acknowledgements

The contributions from each author are listed below: (*a*) conceptualization, (*b*) methodology, (*c*) software, (*d*) data analysis and modelling, (*e*) investigation, (*f*) resources, (*g*) writing (original draft) and (*h*) writing (review and editing). AFS (*acdefgh*), PAC (*abcdeh*), DSK (*abcdeh*), JSOE (*acdefh*), FB (*acdefh*), AG (*adefh*), LJS (*cdefh*), EAH (*edfh*), ABB (*cdefh*), RSS (*defh*), AD (*bef*), CP (*c*), BDK (*e*), AP (*e*), IU (*f*), KGM (*df*), TAB (*c*), VK (*efh*), WL (*e*), ALG (*abef*), BBI (*abfh*), CC (*ef*), ESB (*eh*), KMØJ (*abefh*), EEM (*bef*), RBN (*abdef*), IR (*ab*), JSW (*ab*), MA (*beh*), UB (*a*), EB (*ce*), CC (*e*), VC (*bh*), SG (*be*), HH (*be*), OSH (*bce*), ZK (*e*), NK (*e*), TM (*c*), MN (*beh*), AP (*b*), TRP (*abeh*), LR (*e*), MR (*b*), AS (*b*), CS (*bef*), MT (*e*), PT (*b*), UZ (*b*), KA (*abdefh*), DAK (*abdefgh*). We acknowledge European XFEL in Schenefeld, Germany, for the provision of XFEL beam time at Scientific Instrument HED (High Energy Density Science) (proposal Nos. 3248 and 7136). I15-1 data in Fig. 9 were collected by Daniel Irving as part of the I15-1 mail-in service (proposal CY39017), Diamond Light Source. We are grateful to Antonio Cervellino for collecting the SLS (PSI, Switzerland) synchrotron data plotted in Fig. 9 for DAK in 2010. Parts of this research were carried out at PETRA III and we would like to thank Martin Aaskov Karlsen for assistance in using beamline P02.1. Beam time was allocated for proposal I-20230990 EC. The authors acknowledge MAX IV Laboratory for time on Beamline DanMAX (proposal No. 20231682) and would like to thank Mads R. V. Jørgensen and Frederik H. Gjørup for their assistance. We thank Stefan Kycia (University of Guelph) for useful discussions about the inclined Varex detector arrangement. We thank Theo Maltezopoulos for his work enabling the XGM to operate at high photon energies and Frank Brinker for making lasing available at 24 keV. The authors are indebted to the HIBEF UC for the provision of instrumentation and staff that enabled this experiment.

Data availability

Experiment archives are available at https://doi.org//10.22003/XFEL.EU-DATA-007316-00 (data presented in the main text) and https://doi.org//10.22003/XFEL.EU-DATA-003248-00 (data presented in Appendix *A*).

Funding information

We acknowledge DESY (Hamburg, Germany), a member of the Helmholtz Association HGF, for the provision of experimental facilities. Research conducted at MAX IV is supported by the Swedish Research Council under contract 2018-07152, the Swedish Governmental Agency for Innovation Systems under contract 2018-04969 and Formas under contract 2019-02496. DanMAX is funded by the NUFI grant No. 4059-00009B. AFS, RSS and KMØJ thank the Villum Foundation (42079), the Danish National Research Foundation (DNRF149) and the Novo Nordisk Foundation (0085640) for funding. The authors also thank the Danish Agency for Science, Technology, and Innovation for funding the instrument centre DanScatt. LJS, ABB, VAK and BBI thank the Villum Foundation (25861). EAH thanks the UK Hub for the Physical Sciences on XFELS (HPSX) for part-funding her DPhil Studentship. CC (Crepisson) acknowledges support from the UK Engineering and Physical Sciences Research Council (EPSRC) under grant Nos. EP/W010097/1 and EP/P015794/1. MF acknowledges support from the UK EPSRC under Grant No. EP/X025373/1 and Amplifi PP. ESB was supported by the European Union's Horizon Europe research and innovation programme under grant agreement No. 101185375. This work was supported by the UK Research & Innovation Future Leaders Fellowship (grant No. MR/W008211/1 awarded to EEM). JSW gratefully acknowledges support from EPSRC under research grant EP/X031624/1. TS appreciates support from AWE *via* the Oxford Centre for High Energy Density Science (OxCHEDS). CC (Camarda) acknowledges funding by the Deutsche Forschungsgemeinschaft (DFG, German Research Foundation) under contract No. 521549147 in grant No. AP262/3-1, DFG Priority program Deep Dyn SPP 2404.

References

Afanasiev, D. & Kimel, A. V. (2023). *Nat. Mater.* **22**, 673–674.
Appleby, G. A., Pascarelli, S., Pahl, D. **&** and Tschentscher, T. (2017). *Synchrotron Radiat. News* **30**, 6–8.
Ashiotis, G., Deschildre, A., Nawaz, Z., Wright, J. P., Karkoulis, D., Picca, F. E. & Kieffer, J. (2015). *J. Appl. Cryst.* **48**, 510–519.

Bertolotti, F., Vivani, A., Moscheni, D., Ferri, F., Cervellino, A., Masciocchi, N. & Guagliardi, A. (2020). *Nanomaterials* **10**, 743.
Bigot, J.-Y., Vomir, M. & Beaurepaire, E. (2009). *Nat. Phys.* **5**, 515–520.
Blanton, T. N., Rajeswaran, M., Stephens, P. W., Whitcomb, D. R., Misture, S. T. & Kaduk, J. A. (2011). *Powder Diffr.* **26**, 313–320.
Burns, N., Rahemtulla, A., Annett, S., Moreno, B. & Kycia, S. (2023). *J. Appl. Cryst.* **56**, 510–518.
Cervellino, A., Frison, R., Bertolotti, F. & Guagliardi, A. (2015). *J. Appl. Cryst.* **48**, 2026–2032.
Christiansen, T. L., Cooper, S. & Jensen, Ø. (2020). *Nanoscale Adv.* **2**, 2234–2254.
Coelho, A. A. (2018). *J. Appl. Cryst.* **51**, 210–218.
Decking, W., Abeghyan, S., Abramian, P., Abramsky, A., Aguirre, A., Albrecht, C., Alou, P., Altarelli, M., Altmann, P., Amyan, K., Anashin, V., Apostolov, E., Appel, K., Auguste, D., Ayvazyan, V., Baark, S., Babies, F., Baboi, N., Bak, P., Balandin, V., Baldinger, R., Baranasic, B., Barbanotti, S., Belikov, O., Belokurov, V., Belova, L., Belyakov, V., Berry, S., Bertucci, M., Beutner, B., Block, A., Blöcher, M., Böckmann, T., Bohm, C., Böhnert, M., Bondar, V., Bondarchuk, E., Bonezzi, M., Borowiec, P., Bösch, C., Bösenberg, U., Bosotti, A., Böspflug, R., Bousonville, M., Boyd, E., Bozhko, Y., Brand, A., Branlard, J., Briechle, S., Brinker, F., Brinker, S., Brinkmann, R., Brockhauser, S., Brovko, O., Brück, H., Brüdgam, A., Butkowski, L., Büttner, T., Calero, J., Castro-Carballo, E., Cattalanotto, G., Charrier, J., Chen, J., Cherepenko, A., Cheskidov, V., Chiodini, M., Chong, A., Choroba, S., Chorowski, M., Churanov, D., Cichalewski, W., Clausen, M., Clement, W., Cloué, C., Cobos, J. A., Coppola, N., Cunis, S., Czuba, K., Czwalinna, M., D'Almagne, B., Dammann, J., Danared, H., de Zubiaurre Wagner, A., Delfs, A., Delfs, T., Dietrich, F., Dietrich, T., Dohlus, M., Dommach, M., Donat, A., Dong, X., Doynikov, N., Dressel, M., Duda, M., Duda, P., Eckoldt, H., Ehsan, W., Eidam, J., Eints, F., Engling, C., Englisch, U., Ermakov, A., Escherich, K., Eschke, J., Saldin, E., Faesing, M., Fallou, A., Felber, M., Fenner, M., Fernandes, B., Fernández, J. M., Feuker, S., Filippakopoulos, K., Floettmann, K., Fogel, V., Fontaine, M., Francés, A., Martin, I. F., Freund, W., Freyermuth, T., Friedland, M., Fröhlich, L., Fusetti, M., Fydrych, J., Gallas, A., García, O., Garcia-Tabares, L., Geloni, G., Gerasimova, N., Gerth, C., Geßler, P., Gharibyan, V., Gloor, M., Głowinkowski, J., Goessel, A., Gołębiewski, Z., Golubeva, N., Grabowski, W., Graeff, W., Grebentsov, A., Grecki, M., Grevsmuehl, T., Gross, M., Grosse-Wortmann, U., Grünert, J., Grunewald, S., Grzegory, P., Feng, G., Guler, H., Gusev, G., Gutierrez, J. L., Hagge, L., Hamberg, M., Hanneken, R., Harms, E., Hartl, I., Hauberg, A., Hauf, S., Hauschildt, J., Hauser, J., Havlicek, J., Hedqvist, A., Heidbrook, N., Hellberg, F., Henning, D., Hensler, O., Hermann, T., Hidvégi, A., Hierholzer, M., Hintz, H., Hoffmann, F., Hoffmann, M., Hoffmann, M., Holler, Y., Hüning, M., Ignatenko, A., Ilchen, M., Iluk, A., Iversen, J., Iversen, J., Izquierdo, M., Jachmann, L., Jardon, N., Jastrow, U., Jensch, K., Jensen, J., Jeżabek, M., Jidda, M., Jin, H., Johansson, N., Jonas, R., Kaabi, W., Kaefer, D., Kammering, R., Kapitza, H., Karabekyan, S., Karstensen, S., Kasprzak, K., Katalev, V., Keese, D., Keil, B., Kholopov, M., Killenberger, M., Kitaev, B., Klimchenko, Y., Klos, R., Knebel, L., Koch, A., Koepke, M., Köhler, S., Köhler, W., Kohlstrunk, N., Konopkova, Z., Konstantinov, A., Kook, W., Koprek, W., Körfer, M., Korth, O., Kosarev, A., Kosiński, K., Kostin, D., Kot, Y., Kotarba, A., Kozak, T., Kozak, V., Kramert, R., Krasilnikov, M., Krasnov, A., Krause, B., Kravchuk, L., Krebs, O., Kretschmer, R., Kreutzkamp, J., Kröplin, O., Krzysik, K., Kube, G., Kuehn, H., Kujala, N., Kulikov, V., Kuzminych, V., La Civita, D., Lacroix, M., Lamb, T., Lancetov, A., Larsson, M., Le Pinvidic, D., Lederer, S., Lensch, T., Lenz, D., Leuschner, A., Levenhagen, F., Li, Y., Liebing, J., Lilje, L., Limberg, T., Lipka, D., List, B., Liu, J., Liu, S., Lorbeer, B., Lorkiewicz, J., Lu, H. H., Ludwig, F., Machau, K., Maciocha, W., Madec, C., Magueur, C., Maiano, C., Maksimova, I., Malcher, K., Maltezopoulos, T., Mamoshkina, E., Manschwetus, B., Marcellini, F., Marinkovic, G., Martinez, T., Martirosyan, H., Maschmann, W., Maslov, M., Matheisen, A., Mavric, U., Meißner, J., Meissner, K., Messerschmidt, M., Meyners, N., Michalski, G., Michelato, P., Mildner, N., Moe, M., Moglia, F., Mohr, C., Mohr, S., Möller, W., Mommerz, M., Monaco, L., Montiel, C., Moretti, M., Morozov, I., Morozov, P., Mross, D., Mueller, J., Müller, C., Müller, J., Müller, K., Munilla, J., Münnich, A., Muratov, V., Napoly, O., Näser, B., Nefedov, N., Neumann, R., Neumann, R., Ngada, N., Noelle, D., Obier, F., Okunev, I., Oliver, J. A., Omet, M., Oppelt, A., Ottmar, A., Oublaid, M., Pagani, C., Paparella, R., Paramonov, V., Peitzmann, C., Penning, J., Perus, A., Peters, F., Petersen, B., Petrov, A., Petrov, I., Pfeiffer, S., Pflüger, J., Philipp, S., Pienaud, Y., Pierini, P., Pivovarov, S., Planas, M., Pławski, E., Pohl, M., Polinski, J., Popov, V., Prat, S., Prenting, J., Priebe, G., Pryschelski, H., Przygoda, K., Pyata, E., Racky, B., Rathjen, A., Ratuschni, W., Regnaud-Campderros, S., Rehlich, K., Reschke, D., Robson, C., Roever, J., Roggli, M., Rothenburg, J., Rusiński, E., Rybaniec, R., Sahling, H., Salmani, M., Samoylova, L., Sanzone, D., Saretzki, F., Sawlanski, O., Schaffran, J., Schlarb, H., Schlösser, M., Schlott, V., Schmidt, C., Schmidt-Foehre, F., Schmitz, M., Schmökel, M., Schnautz, T., Schneidmiller, E., Scholz, M., Schöneburg, B., Schultze, J., Schulz, C., Schwarz, A., Sekutowicz, J., Sellmann, D., Semenov, E., Serkez, S., Sertore, D., Shehzad, N., Shemarykin, P., Shi, L., Sienkiewicz, M., Sikora, D., Sikorski, M., Silenzi, A., Simon, C., Singer, W., Singer, X., Sinn, H., Sinram, K., Skvorodnev, N., Smirnow, P., Sommer, T., Sorokin, A., Stadler, M., Steckel, M., Steffen, B., Steinhau-Kühl, N., Stephan, F., Stodulski, M., Stolper, M., Sulimov, A., Susen, R., Świerblewski, J., Sydlo, C., Syresin, E., Sytchev, V., Szuba, J., Tesch, N., Thie, J., Thiebault, A., Tiedtke, K., Tischhauser, D., Tolkiehn, J., Tomin, S., Tonisch, F., Toral, F., Torbin, I., Trapp, A., Treyer, D., Trowitzsch, G., Trublet, T., Tschentscher, T., Ullrich, F., Vannoni, M., Varela, P., Varghese, G., Vashchenko, G., Vasic, M., Vazquez-Velez, C., Verguet, A., Vilcins-Czvitkovits, S., Villanueva, R., Visentin, B., Viti, M., Vogel, E., Volobuev, E., Wagner, R., Walker, N., Wamsat, T., Weddig, H., Weichert, G., Weise, H., Wenndorf, R., Werner, M., Wichmann, R., Wiebers, C., Wiencek, M., Wilksen, T., Will, I., Winkelmann, L., Winkowski, M., Wittenburg, K., Witzig, A., Wlk, P., Wohlenberg, T., Wojciechowski, M., Wolff-Fabris, F., Wrochna, G., Wrona, K., Yakopov, M., Yang, B., Yang, F., Yurkov, M., Zagorodnov, I., Zalden, P., Zavadtsev, A., Zavadtsev, D., Zhirnov, A., Zhukov, A., Ziemann, V., Zolotov, A., Zolotukhina, N., Zummack, F. & Zybin, D. (2020). *Nat. Photon.* **14**, 391–397.
Egami, T. & Billinge, S. J. L. (2003). *Underneath the Bragg peaks: structural analysis of complex materials*. Elsevier.
Emma, P., Akre, R., Arthur, J., Bionta, R., Bostedt, C., Bozek, J., Brachmann, A., Bucksbaum, P., Coffee, R., Decker, F.-J., Ding, Y., Dowell, D., Edstrom, S., Fisher, A., Frisch, J., Gilevich, S., Hastings, J., Hays, G., Hering, P., Huang, Z., Iverson, R., Loos, H., Messerschmidt, M., Miahnahri, A., Moeller, S., Nuhn, H.-D., Pile, G., Ratner, D., Rzepiela, J., Schultz, D., Smith, T., Stefan, P., Tompkins, H., Turner, J., Welch, J., White, W., Wu, J., Yocky, G. & Galayda, J. (2010). *Nat. Photon.* **4**, 641–647.
Farrow, C. L., Juhas, P., Liu, J. W., Bryndin, D., Božin, E. S., Bloch, J., Proffen, T. & Billinge, S. J. L. (2007). *J. Phys. Condens. Matter* **19**, 335219.
Georgescu, I. (2020). *Nat. Rev. Phys.* **2**, 345–345.
Gorman, M. G., McGonegle, D., Smith, R. F., Singh, S., Jenkins, T., McWilliams, R. S., Albertazzi, B., Ali, S. J., Antonelli, L., Armstrong, M. R., Baehtz, C., Ball, O. B., Banerjee, S., Belonoshko, A. B., Benuzzi-Mounaix, A., Bolme, C. A., Bouffetier, V., Briggs, R., Buakor, K., Butcher, T., Di Dio Cafiso, S., Cerantola, V., Chantel, J., Di Cicco, A., Clarke, S., Coleman, A. L., Collier, J., Collins, G. W., Comley, A. J., Coppari, F., Cowan, T. E., Cristoforetti, G., Cynn, H., Descamps, A., Dorchies, F., Duff, M. J., Dwivedi, A., Edwards, C., Eggert, J. H., Errandonea, D., Fiquet, G., Galtier, E., Laso Garcia, A., Ginestet, H., Gizzi, L., Gleason, A., Goede, S., Gonzalez, J. M., Harmand, M., Hartley, N. J., Heighway, P. G., Hernandez-Gomez, C., Higginbotham, A., Höppner, H., Husband,

R. J., Hutchinson, T. M., Hwang, H., Lazicki, A. E., Keen, D. A., Kim, J., Koester, P., Konopkova, Z., Kraus, D., Krygier, A., Labate, L., Lee, Y., Liermann, H.-P., Mason, P., Masruri, M., Massani, B., McBride, E. E., McGuire, C., McHardy, J. D., Merkel, S., Morard, G., Nagler, B., Nakatsutsumi, M., Nguyen-Cong, K., Norton, A.-M., Oleynik, I. I., Otzen, C., Ozaki, N., Pandolfi, S., Peake, D. J., Pelka, A., Pereira, K. A., Phillips, J. P., Prescher, C., Preston, T. R., Randolph, L., Ranjan, D., Ravasio, A., Redmer, R., Rips, J., Santamaria-Perez, D., Savage, D. J., Schoelmerich, M., Schwinkendorf, J.-P., Smith, J., Sollier, A., Spear, J., Spindloe, C., Stevenson, M., Strohm, C., Suer, T.-A., Tang, M., Toncian, M., Toncian, T., Tracy, S. J., Trapananti, A., Tschentscher, T., Tyldesley, M., Vennari, C. E., Vinci, T., Vogel, S. C., Volz, T. J., Vorberger, J., Walsh, J. P. S., Wark, J. S., Willman, J. T., Wollenweber, L., Zastrau, U., Brambrink, E., Appel, K. & McMahon, M. I. (2024). *J. Appl. Phys.* **135**, 165902.

Griffiths, J., Suzana, A. F., Wu, L., Marks, S. D., Esposito, V., Boutet, S., Evans, P. G., Mitchell, J. F., Dean, M. P. M., Keen, D. A., Robinson, I., Billinge, S. J. L. & Bozin, E. S. (2024). *Nat. Mater.* **23**, 1041–1047.

Guo, L., Hu, S., Gu, X., Zhang, R., Wang, K., Yan, W. & Sun, X. (2024). *Adv. Mater.* **36**, 2301854.

Hulbert, B. S. & Kriven, W. M. (2023). *J. Appl. Cryst.* **56**, 160–166.

Ishikawa, T., Aoyagi, H., Asaka, T., Asano, Y., Azumi, N., Bizen, T., Ego, H., Fukami, K., Fukui, T., Furukawa, Y., Goto, S., Hanaki, H., Hara, T., Hasegawa, T., Hatsui, T., Higashiya, A., Hirono, T., Hosoda, N., Ishii, M., Inagaki, T., Inubushi, Y., Itoga, T., Joti, Y., Kago, M., Kameshima, T., Kimura, H., Kirihara, Y., Kiyomichi, A., Kobayashi, T., Kondo, C., Kudo, T., Maesaka, H., Maréchal, X. M., Masuda, T., Matsubara, S., Matsumoto, T., Matsushita, T., Matsui, S., Nagasono, M., Nariyama, N., Ohashi, H., Ohata, T., Ohshima, T., Ono, S., Otake, Y., Saji, C., Sakurai, T., Sato, T., Sawada, K., Seike, T., Shirasawa, K., Sugimoto, T., Suzuki, S., Takahashi, S., Takebe, H., Takeshita, K., Tamasaku, K., Tanaka, H., Tanaka, R., Tanaka, T., Togashi, T., Togawa, K., Tokuhisa, A., Tomizawa, H., Tono, K., Wu, S., Yabashi, M., Yamaga, M., Yamashita, A., Yanagida, K., Zhang, C., Shintake, T., Kitamura, H. & Kumagai, N. (2012). *Nat. Photon.* **6**, 540–544.

Jiang, Y., Liu, C., Cao, Z., Li, C., Liu, Z., Wang, C., Xiang, Y. & Zhou, P. (2024). *Nat. Electron.* **7**, 868–875.

Juhás, P., Davis, T., Farrow, C. L. & Billinge, S. J. L. (2013). *J. Appl. Cryst.* **46**, 560–566.

Juhás, P., Farrow, C., Yang, X., Knox, K. & Billinge, S. (2015). *Acta Cryst.* A**71**, 562–568.

Kang, H.-S., Min, C.-K., Heo, H., Kim, C., Yang, H., Kim, G., Nam, I., Baek, S. Y., Choi, H.-J., Mun, G., Park, B. R., Suh, Y. J., Shin, D. C., Hu, J., Hong, J., Jung, S., Kim, S.-H., Kim, K., Na, D., Park, S. S., Park, Y. J., Han, J.-H., Jung, Y. G., Jeong, S. H., Lee, H. G., Lee, S., Lee, S., Lee, W.-W., Oh, B., Suh, H. S., Parc, Y. W., Park, S.-J., Kim, M. H., Jung, N.-S., Kim, Y.-C., Lee, M.-S., Lee, B.-H., Sung, C.-W., Mok, I.-S., Yang, J.-M., Lee, C.-S., Shin, H., Kim, J. H., Kim, Y., Lee, J. H., Park, S.-Y., Kim, J., Park, J., Eom, I., Rah, S., Kim, S., Nam, K. H., Park, J., Park, J., Kim, S., Kwon, S., Park, S. H., Kim, K. S., Hyun, H., Kim, S. N., Kim, S., Hwang, S., Kim, M. J., Lim, C., Yu, C.-J., Kim, B.-S., Kang, T.-H., Kim, K.-W., Kim, S.-H., Lee, H.-S., Lee, H.-S., Park, K.-H., Koo, T.-Y., Kim, D.-E. & Ko, I. S. (2017). *Nat. Photon.* **11**, 708–713.

Keen, D. A. (2001). *J. Appl. Cryst.* **34**, 172–177.

Keen, D. A. (2020). *Crystallogr. Rev.* **26**, 143–201.

Keen, D. A. & Goodwin, A. L. (2015). *Nature* **521**, 303–309.

Kim, K. H., Kim, J. G., Nozawa, S., Sato, T., Oang, K. Y., Kim, T. W., Ki, H., Jo, J., Park, S., Song, C., Sato, T., Ogawa, K., Togashi, T., Tono, K., Yabashi, M., Ishikawa, T., Kim, J., Ryoo, R., Kim, J., Ihee, H. & Adachi, S. (2015). *Nature* **518**, 385–389.

Kohara, S. & Suzuya, K. (2003). *Nucl. Instrum. Methods Phys. Res. B* **199**, 23–28.

Kraus, D., Rips, J., Schörner, M., Stevenson, M. G., Vorberger, J., Ranjan, D., Lütgert, J., Heuser, B., Eggert, J. H., Liermann, H.-P., Oleynik, I. I., Pandolfi, S., Redmer, R., Sollier, A., Strohm, C., Volz, T. J., Albertazzi, B., Ali, S. J., Antonelli, L., Bähtz, C., Ball, O. B., Banerjee, S., Belonoshko, A. B., Bolme, C. A., Bouffetier, V., Briggs, R., Buakor, K., Butcher, T., Cerantola, V., Chantel, J., Coleman, A. L., Collier, J., Collins, G. W., Comley, A. J., Cowan, T. E., Cristoforetti, G., Cynn, H., Descamps, A., Di Cicco, A., Di Dio Cafiso, S., Dorchies, F., Duff, M. J., Dwivedi, A., Edwards, C., Errandonea, D., Galitskiy, S., Galtier, E., Ginestet, H., Gizzi, L., Gleason, A., Göde, S., Gonzalez, J. M., Gorman, M. G., Harmand, M., Hartley, N. J., Heighway, P. G., Hernandez-Gomez, C., Higginbotham, A., Höppner, H., Husband, R. J., Hutchinson, T. M., Hwang, H., Keen, D. A., Kim, J., Koester, P., Konôpková, Z., Krygier, A., Labate, L., Laso Garcia, A., Lazicki, A. E., Lee, Y., Mason, P., Masruri, M., Massani, B., McBride, E. E., McHardy, J. D., McGonegle, D., McGuire, C., McWilliams, R. S., Merkel, S., Morard, G., Nagler, B., Nakatsutsumi, M., Nguyen-Cong, K., Norton, A.-M., Ozaki, N., Otzen, C., Peake, D. J., Pelka, A., Pereira, K. A., Phillips, J. P., Prescher, C., Preston, T. R., Randolph, L., Ravasio, A., Santamaria-Perez, D., Savage, D. J., Schölmerich, M., Schwinkendorf, J.-P., Singh, S., Smith, J., Smith, R. F., Spear, J., Spindloe, C., Suer, T.-A., Tang, M., Toncian, M., Toncian, T., Tracy, S. J., Trapananti, A., Vennari, C. E., Vinci, T., Tyldesley, M., Vogel, S. C., Walsh, J. P. S., Wark, J. S., Willman, J. T., Wollenweber, L., Zastrau, U., Brambrink, E., Appel, K. & McMahon, M. I. (2025). *Nature* **642**, 351–355.

Liu, B. (2022). *Proceedings of the International Linear Accelerator Conference (LINAC2022)*, 28 August – 2 September 2022, Liverpool, UK. TU1AA05.

Magnard, N. P. L., Sørensen, D. R., Kantor, I., Jensen, K. M. Ø. & Jørgensen, M. R. V. (2023). *J. Appl. Cryst.* **56**, 825–833.

Nakano, M., Miyashita, O., Jonic, S., Song, C., Nam, D., Joti, Y. & Tama, F. (2017). *J. Synchrotron Rad.* **24**, 727–737.

Neder, R. B. & Proffen, T. (2020). *J. Appl. Cryst.* **53**, 710–721.

Obara, Y., Ito, H., Ito, T., Kurahashi, N., Thürmer, S., Tanaka, H., Katayama, T., Togashi, T., Owada, S., Yamamoto, Y., Karashima, S., Nishitani, J., Yabashi, M., Suzuki, T. & Misawa, K. (2017). *Struct. Dyn.* **4**, 044033.

Pan, S., Ganss, F., Panda, S., Sellge, G., Banerjee, C., Sinha, J., Hellwig, O. & Barman, A. (2022). *J. Mater. Sci.* **57**, 6212–6222.

Prat, E., Abela, R., Aiba, M., Alarcon, A., Alex, J., Arbelo, Y., Arrell, C., Arsov, V., Bacellar, C., Beard, C., Beaud, P., Bettoni, S., Biffiger, R., Bopp, M., Braun, H.-H., Calvi, M., Cassar, A., Celcer, T., Chergui, M., Chevtsov, P., Cirelli, C., Citterio, A., Craievich, P., Divall, M. C., Dax, A., Dehler, M., Deng, Y., Dietrich, A., Dijkstal, P., Dinapoli, R., Dordevic, S., Ebner, S., Engeler, D., Erny, C., Esposito, V., Ferrari, E., Flechsig, U., Follath, R., Frei, F., Ganter, R., Garvey, T., Geng, Z., Gobbo, A., Gough, C., Hauff, A., Hauri, C. P., Hiller, N., Hunziker, S., Huppert, M., Ingold, G., Ischebeck, R., Janousch, M., Johnson, P. J. M., Johnson, S. L., Juranić, P., Jurcevic, M., Kaiser, M., Kalt, R., Keil, B., Kiselev, D., Kittel, C., Knopp, G., Koprek, W., Laznovsky, M., Lemke, H. T., Sancho, D. L., Löhl, F., Malyzhenkov, A., Mancini, G. F., Mankowsky, R., Marcellini, F., Marinkovic, G., Martiel, I., Märki, F., Milne, C. J., Mozzanica, A., Nass, K., Orlandi, G. L., Loch, C. O., Paraliev, M., Patterson, B., Patthey, L., Pedrini, B., Pedrozzi, M., Pradervand, C., Radi, P., Raguin, J.-Y., Redford, S., Rehanek, J., Reiche, S., Rivkin, L., Romann, A., Sala, L., Sander, M., Schietinger, T., Schilcher, T., Schlott, V., Schmidt, T., Seidel, M., Stadler, M., Stingelin, L., Svetina, C., Treyer, D. M., Trisorio, A., Vicario, C., Voulot, D., Wrulich, A., Zerdane, S. & Zimoch, E. (2020). *Nat. Photonics* **14**, 748–754.

Prencipe, I., Fuchs, J., Pascarelli, S., Schumacher, D. W., Stephens, R. B., Alexander, N. B., Briggs, R., Büscher, M., Cernaianu, M. O., Choukourov, A., Marco, M. D., Erbe, A., Fassbender, J., Fiquet, G., Fitzsimmons, P., Gheorghiu, C., Hund, J., Huang, L. G., Harmand, M., Hartley, N. J., Irman, A., Kluge, T., Konopkova, Z., Kraft, S., Kraus, D., Leca, V., Margarone, D., Metzkes, J., Nagai, K., Nazarov, W., Lutoslawski, P., Papp, D., Passoni, M., Pelka, A., Perin, J. P.,

Schulz, J., Smid, M., Spindloe, C., Steinke, S., Torchio, R., Vass, C., Wiste, T., Zaffino, R., Zeil, K., Tschentscher, T., Schramm, U. & Cowan, T. E. (2017). *High Power Laser Sci. Eng.* **5**, e17.
Proffen, T. (2006). *Rev. Mineral. Geochem.* **63**, 255–274.
Redford, S., Andrä, M., Barten, R., Bergamaschi, A., Brückner, M., Chiriotti, S., Dinapoli, R., Fröjdh, E., Greiffenberg, D., Kim, K. S., Lee, J. H., Lopez-Cuenca, C., Meyer, M., Mezza, D., Mozzanica, A., Park, S.-Y., Ruder, C., Schmitt, B., Shi, X., Thattil, D., Tinti, G., Vetter, S. & Zhang, J. (2020). *J. Instrum.* **15**, C02025.
Redford, S., Andrä, M., Barten, R., Bergamaschi, A., Brückner, M., Dinapoli, R., Fröjdh, E., Greiffenberg, D., Lopez-Cuenca, C., Mezza, D., Mozzanica, A., Ramilli, M., Ruat, M., Ruder, C., Schmitt, B., Shi, X., Thattil, D., Tinti, G., Vetter, S. & Zhang, J. (2018). *J. Instrum.* **13**, C01027.
Rousse, A., Rischel, C., Fourmaux, S., Uschmann, I., Sebban, S., Grillon, G., Balcou, P., Förster, E., Geindre, J. P., Audebert, P., Gauthier, J. C. & Hulin, D. (2001). *Nature* **410**, 65–68.
Schmid, S. W., Pósa, L., Török, T. N., Sánta, B., Pollner, Z., Molnár, G., Horst, Y., Volk, J., Leuthold, J., Halbritter, A. & Csontos, M. (2024). *ACS Nano* **18**, 21966–21974.
Simonov, A. & Goodwin, A. L. (2020). *Nat. Rev. Chem.* **4**, 657–673.
Soper, A. K. (2011). *GudrunN and GudrunX: programs for correcting raw neutron and X-ray diffraction data to differential scattering cross section*. Technical Report RAL-TR-2011-013. Science and Technology Facilities Council, Swindon, UK. https://epubs.stfc.ac.uk/manifestation/6710/RAL-TR-2011-013.pdf.
Soper, A. K. (2013). *ISRN Phys. Chem.* **2013**, 279463.
Soper, A. K. & Barney, E. R. (2011). *J. Appl. Cryst.* **44**, 714–726.
Støckler, L. J., Christensen, R. S., Kløve, M., Bertelsen, A. D., Borup, A. B., Krause, L., Takahashi, S., Fujita, T., Kasai, H., Inoue, I., Nishibori, E. & Iversen, B. B. (2023). *ChemPhysChem* **24**, e202300407.
Støckler, L. J., Krause, L., Svane, B., Tolborg, K., Richter, B., Takahashi, S., Fujita, T., Kasai, H., Sugahara, M., Inoue, I., Nishibori, E. & Iversen, B. B. (2023). *IUCrJ* **10**, 103–117.
Terban, M. W. & Billinge, S. J. L. (2022). *Chem. Rev.* **122**, 1208–1272.
Tschentscher, T., Bressler, C., Grünert, J., Madsen, A., Mancuso, A. P., Meyer, M., Scherz, A., Sinn, H. & Zastrau, U. (2017). *Appl. Sci.* **7**, 592.
Tucker, M. G., Keen, D. A., Dove, M. T., Goodwin, A. L. & Hui, Q. (2007). *J. Phys. Condens. Matter* **19**, 335218.
Weißenhofer, M. & Oppeneer, P. M. (2024). *Adv. Phys. Res.* 2300103.
Yashima, M. & Takizawa, T. (2010). *J. Phys. Chem. C* **114**, 2385–2392.
Yasuda, K., Zalys-Geller, E., Wang, X., Bennett, D., Cheema, S. S., Watanabe, K., Taniguchi, T., Kaxiras, E., Jarillo-Herrero, P. & Ashoori, R. (2024). *Science* **385**, 53–56.
Zastrau, U., Appel, K., Baehtz, C., Baehr, O., Batchelor, L., Berghäuser, A., Banjafar, M., Brambrink, E., Cerantola, V., Cowan, T. E., Damker, H., Dietrich, S., Di Dio Cafiso, S., Dreyer, J., Engel, H.-O., Feldmann, T., Findeisen, S., Foese, M., Fulla-Marsa, D., Göde, S., Hassan, M., Hauser, J., Herrmannsdörfer, T., Höppner, H., Kaa, J., Kaever, P., Knöfel, K., Konôpková, Z., Laso García, A., Liermann, H.-P., Mainberger, J., Makita, M., Martens, E.-C., McBride, E. E., Möller, D., Nakatsutsumi, M., Pelka, A., Plueckthun, C., Prescher, C., Preston, T. R., Röper, M., Schmidt, A., Seidel, W., Schwinkendorf, J.-P., Schoelmerich, M. O., Schramm, U., Schropp, A., Strohm, C., Sukharnikov, K., Talkovski, P., Thorpe, I., Toncian, M., Toncian, T., Wollenweber, L., Yamamoto, Sh. & Tschentscher, T. (2021). *J. Synchrotron Rad.* **28**, 1393–1416.